Universität Bremen

Modelling of the End of Last Ice Age in Transient Framework with a Coupled Climate Model

By

Yuchen Sun

DISSERTATION

Submitted to the University of Bremen
in accordance with the requirements of the degree of
DOCTOR OF NATURAL SCIENCES.

Department of Physics
UNIVERSITY OF BREMEN
and
Alfred-Wegener-Institute for Polar and Marine Research

Reviewers:

1. Prof. Dr. Gerrit Lohmann
2. Prof. Dr. Xu Zhang

Date of PhD defense:
04.10.2022

Abstract

The last deglaciation was characterized by a sequence of abrupt climate events thought to be linked to rapid changes in Atlantic meridional overturning circulation (AMOC). The sequence includes a weakening of the AMOC after the Last Glacial Maximum (LGM) during Heinrich Stadial 1 (HS1), which ends with an abrupt AMOC recovery giving rise to Bølling/Allerød (B/A) warming. This transition occurs under a background with persistent deglacial meltwater fluxes (MWF) that are deemed to play a negative role in North Atlantic Deep Water (NADW) formation. Using a fully coupled Earth system model COSMOS with a range of deglacial boundary conditions and reconstructed deglacial meltwater fluxes, we show that deglacial CO_2 rise and ice sheet decline modulate the sensitivity of the AMOC to these fluxes. While declining ice sheets increase the sensitivity, increasing atmospheric CO_2 levels tend to counteract this effect. These effects, therefore, might account for the occurrence of abrupt AMOC increase in the presence of meltwater, as an alternative to or in combination with changes in the magnitude and/or distribution of meltwater discharge.

To understand the dynamics of B/A warming, an appropriate Heinrich Stadial ocean state is necessary, which was previously obtained by imposing meltwater flux directly into the key convection sites of the North Atlantic, though without a proper distribution of meltwater flux along continental coasts. Given a more realistic distribution of meltwater flux according to PMIP4 protocol, the HS1-B/A sequence could not be properly reproduced in transient simulations, perhaps due to a reduced freshwater flux during HS1 and significant MPW-1a during B/A. From our transient simulations, the intensity of AMOC is significantly modulated by the amount of freshwater during the HS1-B/A transition and manipulated by the geographic distribution of freshwater injection. Considering only the geographical distribution of freshwater forcing without its temporal variation, our model shows a stadial climate during HS1 and captures the B/A-like AMOC recovery. This B/A-like behavior is characterized by the self-oscillation of the AMOC and is mainly associated with a gradual change in the orbital parameters. The ice sheet decline after the onset of the abrupt change attenuates the North Atlantic Deep Water (NADW) production, and the accelerated melting of the ice sheet after 14.5 ka (thousand calendar years before present) can develop this process, eventually moving the system out of this self-oscillation regime. The rise in atmospheric CO_2 does not offset this trend due to ice sheet retreat.

Publications

Sun, Y., Knorr, G., Zhang, X., Tarasov, L., Barker, S., Werner, M., & Lohmann, G. Ice sheet decline and rising atmospheric CO_2 control AMOC sensitivity to deglacial meltwater discharge. *Global and Planetary Change*, **210**, doi: 10.1016/j.gloplacha.2022.103755 (2022).

Sun, Y. *et al.*, Bølling-Allerød revisited. *To be submitted*.

Wang, X., Carrapa, B., **Sun, Y.**, *et al.* The role of the westerlies and orography in Asian hydroclimate since the late Oligocene. *Geology*, **48**, 728-732, doi: 10.1130/G47400.1 (2020).

Acknowledgement

The thesis was written at the Alfred Wegener Institute of the Helmholtz Centre for Polar and Marine Research in Bremerhaven, where I spent a valuable part of my life.

Words cannot express my gratitude to my professor Dr. Gerrit Lohmann for his invaluable patience and feedback. I could not have undertaken this journey without his dedicated support. His broad perspective always brought me new inspiration when I was stuck in a bottleneck, and his unending love for science and life has always encouraged me forward.

I am deeply indebted to Prof. Dr. Xu Zhang, for his invaluable academic support throughout my PhD research. He patiently guided me to leave my previously familiar field and start research in the unknown world of paleoclimate. His relentless pursuit of truth has also pushed me to become a better me.

This endeavor would not have been possible without Dr. Gregor Knorr, who has always provided constructive and pertinent advice on my PhD work. His insightful thinking in climate dynamics helped me to complete my PhD research effectively.

I am grateful to Dr. Martin Werner for always giving me quick feedback. His broad knowledge of water isotopes and wealth of experience in numerical simulations helped me to complete my PhD project smoothly.

I'd like to recognize Dr. Veronika Gayler, Akil Hossain, Dr. Hu Yang, Dr. Xiaoxu Shi, Dr. Lu Niu, Dr. Christian Stepanek, Dr. Paul Gierz, and the AWI computing center for the helpful discussions and technique supports. I had the pleasure of working with all my former and

current colleagues in the AWI Paleoclimate Dynamics Group for creating an excellent working environment that I entirely enjoyed.

My wife, Shan Xu, is the person I need to thank the most. We share our joys and sorrows. My wife, Shan Xu, is the person I need to thank the most. We share our joys and sorrows. We are each other's best support while studying abroad. I am also very grateful to my parents and in-laws for their long-standing unconditional love and support. It is their love that gives me the strength to move forward.

I thank the graduate school POLMAR in the AWI for providing useful courses on my PhD study.

Author's Declaration

I hereby affirm that: (1) I wrote the thesis without the help of others, (2) I used only those sources and aids cited in the text, and (3) All passages taken from the sources used, whether quoted literally or in context, have been indicated as such.

Bremerhaven, May 2022

Yuchen Sun

CONTENTS

Chapter 1 General Introduction..1

1.1 Background...1

1.2 Objectives and outline of the thesis..4

Chapter 2 General Methods...7

2.1 Model Description...7

2.2 GLAC-1D ice sheet reconstruction..8

Chapter 3 Ice sheet decline and rising atmospheric CO_2 control AMOC sensitivity to deglacial meltwater discharge 13

3.1 Experimental design..13

3.1.1 Equilibrium HS1 experiments...16

3.1.2 Ice sheet and atmospheric CO_2 sensitivity experiments.................20

3.2 Results..21

3.2.1 Mechanism of AMOC recovery..23

3.2.2 CO_2 effect on AMOC recovery threshold..27

3.2.3 Ice Sheet changes and AMOC meltwater sensitivity.......................29

3.3 Discussion and conclusions 32

Chapter 4 Bølling-Allerød revisited...35

4.1 Experimental design..36

4.1.1 Full forcing transient experiments...38

4.1.2 Single forcing transient experiments..41

4.1.3 Water isotope configuration 41

4.2 Results..43

4.2.1 Role of different freshwater histories in B/A warming.....................43

4.2.2 Model-data Comparison..46

4.2.3 B/A warming—an expression of AMOC self-oscillation 48

4.2.4 Govern dynamic of AMOC self-oscillation......................................54

4.3 Discussion and conclusions 57

Chapter 5 Summary and Outlook..61

References...67

List of tables

Table 3.1: Summary of experimental design details of all simulations in this chapter. 15
Table 3.2 Orbital parameters and GHGs in 16ka and LGM 18
Table 4.1 An overview of experimental details for all the simulations in this study 37

List of figures

Fig. 1.1 Millennial-scale climate variability as documented by Greenland ice-core $\delta^{18}O$ (a 1^{st} order proxy for local temperature, North Greenland Ice Core Project members, 2004) reveals abrupt fluctuations between cold (stadial) and warmer (interstadial) conditions. YD: Younger Dryas, B/A: Bølling-Allerød, HS1: Heinrich Stadial 1, LGM: Last Glacial Maximum. Black triangles represent Heinrich events (e.g., HE1). (From Barker & Knorr, 2021) 4
Fig. 2.1 Time evolution of the equivalent sea level change (ESL) calculated from GLAC-1D. 10
Fig. 2.2 Time evolution of the calving fraction in GLAC-1D. 10
Fig. 2.3 Flow chart for the means calculating MWF in GLAC-1D 11
Fig. 3.1 Orography (m) at 16 ka from GLAC-1D in **a)** the Northern Hemisphere and **b)** the Southern Hemisphere. The ice sheet extent is indicated by red lines. In panels **c)** and **d)** the orography anomalies between LGM and 16 ka are shown. The black lines in panels **c)** and **d)** represent the coastline at the LGM. 16
Fig. 3.2 Map of meltwater discharge (meltwater flux in m/yr) in the different simulations at **a)** 16 ka, **b)** 15.4 ka, **c)** 15.2 ka, **d)** 14.9 ka. The meltwater forcing fields consist of two parts: the melt water part of the glacial ice sheets (located at different coastal regions) and the part due to iceberg

melting in the IRD belt of the North Atlantic. The MWF is derived from the GLAC-1D reconstruction. 19

Fig. 3.3 Temporal evolution of the total global (black) meltwater flux (Sv) and the Atlantic contributions by melting (blue) and calving (red) from GLAC-1D between 16ka and 14.6ka. The red stars correspond to the MWF scenarios 1 to 4 in Fig. 3.2 and Table 3. 1. 19

Fig. 3.4 Time evolution of the AMOC (Sv) defined as the maximum value of the stream function below 500 m in the North Atlantic for different sensitivity experiments (cf. Figs. 3.2, 3.3, 3.5 and Table 3.1). The 16KCTL shown here is intercepted from the results in Fig. 3.5 for the model years 300 to 500. 20

Fig. 3.5 Time evolution of the AMOC (Sv) defined as the maximum value of the stream function below 500 m in the North Atlantic for different sensitivity experiments (cf. Figs. 3.2, 3.3 and Table 3.1). 22

Fig. 3.6 AMOC (Sv) for the sensitivity experiments in Fig. 3.5, represented by the average of the last 100 model years. Positive and negative values indicate clockwise and anti-clockwise circulation, respectively. 23

Fig. 3.7 Trend evolution in the three 16-ka experiments with a transient weakening of the AMOC. **a)** Time scales of AMOC index (Sv) on the corresponding experiment. The arrow marks the period which is used to calculate the composite trend in **b)** to **e)**. **b)** precipitation minus evaporation (mm mon^{-1} ka^{-1}), **c)** sea surface temperature (SST, °C ka^{-1}), **d)** sea surface salinity (SSS, psu ka^{-1}) and **e)** sea surface density (kg m^{-3} ka^{-1}). **c)** to **e)** contain an inlet plot for the vertical profiles over the index region NENA as defined by the red rectangle in panel **c)**. 26

Fig. 3.8 Trend evolution in experiment 16K_0.1 between model year 200 to 1100. Zonal mean trends in the Atlantic Ocean for **a)** salinity (psu ka^{-1}) and **b)** temperature (°C ka^{-1}). **c)** Time evolution of AMOC index (Sv, black) and MFT in the upper AMOC brunch at 43°N (Sv, red). **d)** The subsurface (2000m) temperature (°C, red) evolution averaged in the NENA area. Bold lines in **b)** and **d)** represent 50 yr running-mean values. 27

Fig. 3.9 Time evolution of the AMOC index (Sv) for experiments 16K_0.21

and 16K_0.21_CO2 in response to prescribed atmospheric CO_2 changes (dashed grey line). CO_2 gradually increases from 222 to 241ppm in the first 300 years in 16K_0.21_CO2. Experiment 16K_0.21_CO2 starts from model year 2000 of 16K_0.21. 28

Fig. 3.10 Experiment characteristics in 16K_0.21 and 16K_0.21_CO2. **a)** Time evolution of the MFT in the upper brunch of the AMOC at 43°N (Sv), **b)** vertical temperature profile trends, **c)** Atlantic stream function in 16K_0.21_CO2 averaged between 2800 and 2900 model years, **d)** SSS (psu) difference (16K_0.21_CO2 minus 16K_0.21) averaged between model years 3300-3400. Bold solid lines in **a)** are 50 yr running mean values. 29

Fig. 3.11 The time evolution of AMOC index (Sv) in experiment 16K_0.1_0.2_grad with a gradual increase of deglacial meltwater discharge from 0.1 to 0.2 Sv based on pattern of MWF2 is shown in panel **a)**. Panel **b)** shows AMOC changes in the experiments with constant discharge for LGM conditions (LGM_0.1 and LGM_0.18) and LGM conditions, but with reduced ice levels representative of 16 ka (LGM_16KICE+0.1 and LGM_16KICE+0.1). The AMOC stream function (cf. Fig. 3.6) averaged for the last 100 years in LGM_16KICE+0.15 is shown in panel **c)**. 31

Fig. 4.1 Orography (m) at 16 ka from GLAC-1D in the Northern Hemisphere. The ice sheet extent is indicated by red lines. The black lines in represent the coastline at the LGM. 39

Fig. 4.2 Northern Hemisphere orography differences from 16 ka in different time. The black and red lines are same as in Fig. 4.1. 40

Fig. 4.3 Global distribution of simulated annual mean $\delta^{18}O$ values in precipitation **(a)** and ocean surface waters **(b)** at 16 ka. 43

Fig. 4.4 a) NGRIP Greenland ice-core $\delta^{18}O$. **b)** CO_2 volume from Köhler et al., 2017. **c)** Equivalent sea level change calculated from GLAC-1D (black) and far-field relative sea level records from Tahiti (Deschamps et al., 2012) **d)** Temporal evolution of the total global MWF (Sv) used in TRN-full (blue), TRN-FW (black) and repeated TraCE-21ka experiment (red). **e)** Ice-sheet area change in the North America (NA) **f)** Ice-sheet volume change in the NA **g)** Time evolution of the AMOC (Sv) for transient FW (blue), constant FW (black) and repeated TraCE-21ka experiment (red). Bold line in a) represents 50 yr running-mean values. 46

Fig. 4.5 a, c) Simulated NGRIP δ^{18}O in precipitation and surface temperature together with the NGRID ice core data. **b, d)** The NGRIP results of each experimental simulation were aligned to the time when the B/A transition occurred, respectively. Bold lines represent 50 yr running-mean values. 48

Fig. 4.6 Time evolution of the AMOC (Sv) for the sensitivity experiments. All the experiments shown here contain the same freshwater forcing applied in TRN-FW **a)** Equilibrium run under 16 ka boundaries. **b)** Transient experiments considering both GHG and ice-sheet change. **c)** Transient experiments considering only insolation change. **d)** Transient experiments considering all forcing. **e-g)** equilibrium runs branched from 15ka, 14.8ka and 14.6ka in TRN-FW, respectively. 51

Fig. 4.7 Similar to Fig. 4.6. **a)** Transient experiments considering only GHG change. **b)** Transient experiments considering only ice-sheet extent change. **c)** Transient experiments considering complete ice-sheet change. 52

Fig. 4.8 (a-d) AMOC abrupt change dynamics in the experiments shown in Fig.4.6 (a-d), respectively. SST, SIC and subsurface T are calculated as the regional averages of the NENA (30°W-20°W, 56°-64°N). 53

Fig. 4.9 a) Time evolution of the AMOC (Sv) for TRN-FW. Letters A-D define different time period in the simulation. **(b-e)** Temperature anomaly during different phase of TRN-FW (letters shown in panel **a)**) in the Atlantic section. **b)** 15.2ka minus 16ka; **c)** 14.9ka minus 15.2ka; **d)** 14.6ka minus 14.9ka; **e)** 14.4ka minus 14.6ka 54

Fig. 4.10 Zonal mean wind stress (Pa) anomaly along 100°W-40°W in TRN-FW-ICEGHG. Contour shows zonal mean wind stress. The data is smoothed by 10 yr running-mean. 56

Fig. 4.11 a-c) Simulated mixed layer depth in TRN-FW-ICEGHG at 15.1ka **(a)**, 13.6ka **(b)**, and the anomaly between these two times (c); **d-f)** same as **a-c)**, but for sea ice compactness; **g-i)** same as **a-c)**, but for sea surface salinity.. 57

Abbreviation

AMOC	Atlantic Meridional Overturning Circulation
AOGCM	Atmosphere-Ocean General Circulation Model
B/A	Bølling/Allerød
D-O	Dansgaard-Oeschger
ESL	Equivalent Sea Level
ESM	Earth System Model
GHG	Greenhouse Gas
HS1	Heinrich Stadial 1
IRD	Ice-Rafted Debris
ITCZ	Intertropical Convergence Zone
ka	thousand calendar years before present
LGM	Last Glacial Maximum
LIS	Laurentide Ice Sheet
MFT	Meridional Freshwater Transport
MWF	Meltwater Fluxes
NA	North Atlantic Ocean
NAC	North Atlantic Current
NADW	North Atlantic Deep Water
NENA	Northeastern North Atlantic
NGRIP	North Greenland Ice Core Project
SSOP	Subgrid Scale Orographic Parameterization
SSS	Sea Surface Salinity
SST	Sea Surface Temperature
Sv	Sverdrup
T1	Termination 1
V-SMOW	Vienna Standard Mean Ocean Water standard
WSNA	Western Subtropical North Atlantic

Chapter 1 General Introduction

1.1 Background

Glacial to interglacial climate transitions, also known as Glacial Termination, represent the largest global-scale climate variations during the Quaternary. These glacial terminations are characterized by a high degree of climate internal non-linearity since their origin has been linked to a relatively modest gradual changes in external insolation forcing (Imbrie et al. 1993; Raymo et al. 1997). It has been acknowledged that a key to understanding the diversity of deglaciation regarding its shape and rapidity (e.g., Denton et al. 2010; Barker and Knorr, 2021) is associated with abrupt change in the Atlantic Meridional Overturning Circulation (AMOC).

The AMOC is characterized by a net northward flow of warm thermocline and intermediate waters occurs in the upper ocean (1 km) throughout the Atlantic basin. It is compensated by a net southward flow of colder North Atlantic Deep Water (NADW) originating from the Labrador and Nordic Seas at depths between approximately 1 and 3 km. As part of the Global Meridional Overturning Circulation (GMOC), this global "conveyor belt" redistributes large amounts of heat and salt across all oceans and also plays a key role in the carbon cycle. The millennial-scale oscillation of the AMOC (Böhm et al. 2015; Deany et al, 2017; Venz et al. 1999; Barker et al. 2011) is likely to result in large amplitude transitions between cold stadial and warm interstadial states known as “Dansgaard-Oeschger (D-O) oscillations” (Dansgaard et al., 1993) during the last glacial period. Specifically, a sequence of climatic events during the end of last ice age, has led to much debate regarding a mechanistic understanding of terminations in general.

The abrupt AMOC amplification at the beginning of the Bølling/Allerød (B/A) interstadial after a reduced AMOC phase during Heinrich Stadial 1 (HS1) has especially challenged our understanding of abrupt climate changes in face of progressive ice sheet disintegration (Fig. 1.1). The HS1-B/A transition (about 14.7 to 14.2 ka, Ivanovic et al., 2016) was characterized by abrupt and drastic warming in Greenland (10 °C within a few decades, Buizert et al., 2014). During the B/A interval (about 14.7 to 13 ka), the warming trend in Antarctica and the Southern Hemisphere stopped and turned into a cooling trend (Pedro et al., 2016). In recent decades, scientists focused on the variations in AMOC stability to explain the associated abrupt climate changes (e.g., Lohmann and Schulz, 2000; Knorr and Lohmann, 2003; Ganopolski and Roche, 2009; Barker and Knorr, 2021). In addition, some numerical simulations perfectly match the proxy records by artificially adjusting the spatiotemporal variations in meltwater input to the North Atlantic midway through the last deglaciation (e.g., Liu et al. 2009; Menviel et al. 2011).

For example, an abrupt AMOC strengthening is related to a cessation of North Atlantic meltwater discharge in deglacial transient experiments (He et al., 2013; Liu et al., 2009; Menviel et al., 2011). While other modeling studies suggested that abrupt AMOC recovery is associated with gradual global warming (Knorr and Lohmann, 2007; Barker and Knorr, 2007; Dima et al. 2018). It has been demonstrated that atmospheric CO_2 and ice sheet height can modulate its strength (Galbraith and Lavergne, 2019; Oka et al. 2012; Muglia and Schmittner, 2015; Klockmann et al. 2016; Scherriff-Tadano et al. 2018) and its abrupt change of the AMOC (Zhang et al., 2014; 2017; Banderas et al. 2015; Klockmann et al. 2018). In particular, a recent fully coupled atmosphere-ocean general circulation model (AOGCM) study (Obase and Abe-Ouchi, 2019) has shown that an abrupt AMOC can occur without reduction or cessation of glacial meltwater to the North

Atlantic, accounting for B/A warming. In this scenario gradual deglacial warming weakens stratification in the North Atlantic, causing a rapid retreat of sea ice and initiation of deep-water formation. However, in spite of simulating a B/A-like event, the initial deglacial AMOC reduction after the Last Glacial Maximum (LGM, ~21ka) is not captured in Obase and Abe-Ouchi (2019). In this context, the fixed LGM ice sheet conditions used might be critical, as a declining Northern Hemisphere ice sheets might have altered the stability properties of the AMOC (Zhang et al. 2014) and weakened the strength of the AMOC during deglaciation (Zhu et al. 2014).

A recent study proposed that occurrences of millennial-scale abrupt climate changes in glacial cycles are associated with a nonlinear response to structural changes in the stability of the AMOC due to changes in atmospheric CO_2 and continental ice volume (Barker & Knorr, 2021). Specifically, the B/A event occurs as a result of the rise in CO_2 during Heinrich Stadial 1 (HS1), forcing the system towards a monostable strong scheme. And this mechanism remains working in the presence of freshwater forcing. However, this concept about the B/A occurrence has not been verified through numerical simulations. Due to the uncertainty of sea-level reconstruction, we cannot be sure of the effect of ice volume reduction against CO_2 rise. We also don't know whether this theory still holds in the presence of strong freshwater forcing during the HS1-B/A transition. Thus, transient experiments with a fully coupled Earth System Model (ESM) are highly desirable to disentangle the effect of different boundary conditions associated with AMOC changes.

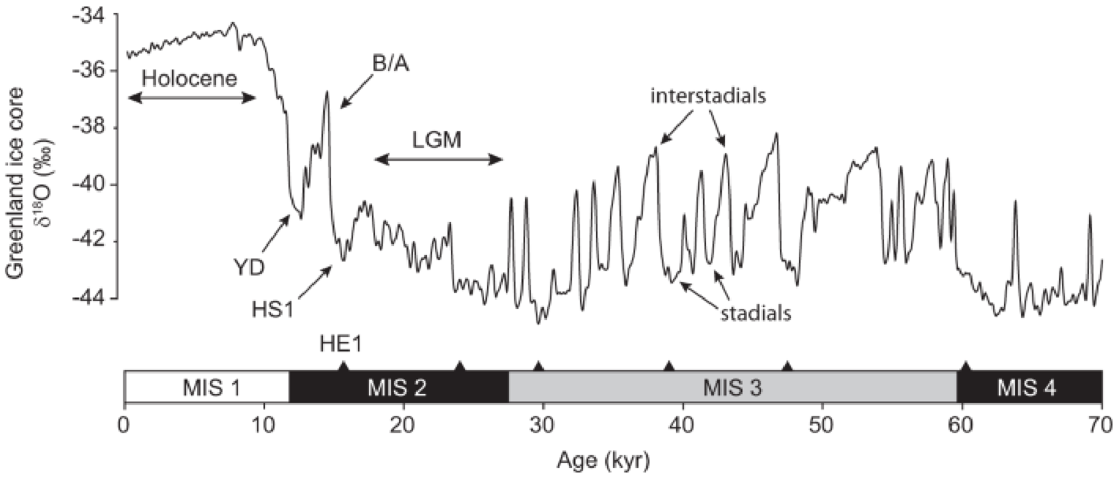

Fig. 1.1 Millennial-scale climate variability as documented by Greenland ice-core $\delta^{18}O$ (a 1st order proxy for local temperature, North Greenland Ice Core Project members, 2004) reveals abrupt fluctuations between cold (stadial) and warmer (interstadial) conditions. YD: Younger Dryas, B/A: Bølling-Allerød, HS1: Heinrich Stadial 1, LGM: Last Glacial Maximum. Black triangles represent Heinrich events (e.g., HE1). (From Barker & Knorr, 2021)

1.2 Objectives and outline of the thesis

There are several specific questions addressed in this thesis:

1. What are the implications of changes in ice sheet and CO_2 for the AMOC strength during the end of the last ice age?

   Previous studies have shown an abrupt AMOC strengthening in deglacial model experiments by a cessation of North Atlantic meltwater discharge. However other model investigations suggested that abrupt AMOC transitions can be directly triggered by gradual boundary condition change. We examine the impact of changes in two key boundary conditions - ice sheets and atmospheric CO_2 concentration - on the abrupt climate change during the LGM-HS1-B/A period through a series of sensitivity experiments in Chapter 3.

2. What is the response of climate model to reconstructed freshwater forcing resulting from ice sheet retreat?

When introducing freshwater forcing to ocean models, many studies have chosen to inject freshwater directly into the deep-water formation area or Ruddiman belt to mimic the melting ice bergs (e.g., Manabe and Stouffer, 1997; Peltier et al., 2006; Otto-Bliesner and Brady, 2010). Indeed, in addition to icebergs, a large amount of freshwater enters the ocean as surface runoff. If only the form of calving is considered, the impact of freshwater on deep water production may be overestimated. This thesis implements a distribution of freshwater due to melting and calving in all freshwater forcing experiments in Chapter 3 and Chapter 4. In addition, transient simulations from late HS1 to B/A are performed using the reconstructed freshwater scenarios in this scheme in Chapter 4.

3. How does strength of AMOC respond to simultaneous changes in ice sheets and CO_2? Do changes in other boundary conditions also play a role during this period?

According to Barker and Gregor (2021), during the period of HS1 increasing atmospheric CO_2 would overcome the effect exerted by declining ice sheet height on AMOC stability, triggering a recovery of AMOC by forcing AMOC towards a monostable strong (B/A) state. In Chapter 3, we considered the effects of rising CO_2 and declining ice sheet on AMOC separately, but did not consider both factors simultaneously, and therefore could not test this hypothesis. In Chapter 4, we performed full transient experiments with simultaneous changes in both ice sheet and CO_2 according to reconstructions. In addition, we conducted sensitivity transient experiments to test single and combined roles of deglacial boundary conditions (i.e., ice sheet height, ice sheet extent, atmospheric CO_2 and orbital parameters) in simulating HS1-B/A.

4. What is the mechanism for the occurrence of B/A event?

   With a series of sensitivity experiments on the HS1-B/A transition, we propose a new hypothesis for the occurrence of B/A in Chapter 4.

The general structure of this thesis is as follows. Chapter 2 provides the general methodology employed in the two main studies presented in Chapter 3 and Chapter 4. Chapter 5 summarizes the main findings of the thesis and provides an outlook for possible future research.

In more detail: In Chapter 2, a fully coupled ocean-atmosphere-sea ice-land surface model COSMOS which is used in Chapter 3 and 4 is introduced at first. A state-of-the-art ice sheet reconstruction dataset GLAC-1D and the associated freshwater fluxes (Tarasov et al., 2012; Briggs et al., 2014; Tarasov et al., 2014) which are used for all the experiments in this thesis are presented. Furthermore, we describe the key technical issues of model setup in transient experiments used in Chapter 4. Chapter 3 is based on a manuscript published in Global and Planetary Change (Sun et al., 2022), the question 1 is answered through a set of sensitivity experiments using boundary conditions of LGM and late H1 based on ice sheet and freshwater reconstructions. This is followed by Chapter 4: full forcing transient experiments in the end of last ice age. Questions 2 to 4 are discussed in detail in this chapter. This work is to be submitted (Sun et al. in prep). Finally, the summary and outlook of this thesis is provided in Chapter 5.

Chapter 2 General Methods

2.1 Model Description

We use the fully-coupled ocean-atmosphere-sea ice-land surface model COSMOS (Jungclaus et al., 2006). The ocean component MPI-OM (Marsland et al., 2003) including a dynamic sea-ice model (Hibler, 1979) and has a formal horizontal resolution of GR30 (3°×1.8°), with 40 uneven vertical layers. The MPI-OM set-up has a bipolar orthogonal spherical coordinate system, where the poles are placed over Greenland and Antarctica, respectively. The atmospheric component ECHAM5 (Röckner et al., 2003) runs at a horizontal resolution of ~3.75° × 3.75° with 19 vertical levels and is complemented by the land surface scheme JSBACH (Raddatz et al., 2007) including a dynamical vegetation module (Brovkin et al., 2009). Within COSMOS, atmosphere and ocean are coupled via the Ocean-Atmosphere-Sea Ice-Soil (OASIS3) coupler (Valcke et al., 2003). Mass, energy, and momentum fluxes, are exchanged between the atmosphere and ocean once per day. The coupling is described in detail in Jungclaus et al. (2006).

The climate model has already been used to simulate the past millennium (Jungclaus et al., 2010), the Miocene warm climate (Knorr et al., 2011; Knorr and Lohmann, 2014; Huang et al., 2017; Hossain et al. 2020), the Pliocene (Stepanek et al., 2020; Lohmann et al., 2022), internal variability of the climate system (Wei et al., 2012), Holocene variability (Wei and Lohmann, 2012), the Last Glacial Maximum (LGM) climate (Zhang et al., 2013; Abelmann et al., 2015) and glacial millennial-scale variability (Gong et al., 2013; Zhang et al., 2014; Zhang et al., 2017; Zhang et al., 2021; Knorr et al., 2021). The previous work indicate that the COSMOS model is capable of capturing the nonlinear behavior of the glacial climate system and is thus a very suitable climate model for this study. To provide a direct comparison of water oxygen isotopes between proxy records and model outputs, we used the water-isotope-enabled version of COSMOS that has been used to simulate preindustrial and LGM distributions of $\delta^{18}O$, which are broadly consistent with observations (Werner et al., 2016).

2.2 GLAC-1D ice sheet reconstruction

The orography used in our investigations, is based on the GLAC-1D ice sheet reconstruction (Tarasov et al., 2012; Briggs et al., 2014; Tarasov et al., 2014). All of the GLAC-1D ice-sheet components employ dynamical ice sheet models that have been constrained with multiple proxy indicators and modern observations. In this study, a distribution of freshwater due to melting and calving is implemented in our COSMOS model set-up to study abrupt climate changes during the last deglaciation. The GLAC-1D reconstruction contains not only the extent and thickness of the ice sheet, but also a surface drainage pointer field and approximate partition of solid and liquid discharge at the ice sheet margins. We use this information to distribute the MWF to the corresponding coastal areas. Since GLAC-1D is characterized by a different grid format from ocean component MPI-OM of COSMOS, the original grid points for ice-sheet meltwater drainage is modified to adapt to MPI-OM grid. Here, we refer to the treatment in the ECHAM5 hydrological discharge model (HD model), described in details by Hagemann and Duemenil (1998) and Hagemann and Gates (2003). The HD-model ensures that water flowing into water-sinks over land is redistributed to the ocean. In this way, the ice sheet meltwater calculated from GLAC-1D is redistributed to the nearest coastal ocean grid point.

The magnitude of the global MWF from the ice sheets is calculated by ice volume changes based on 100-year intervals, representing the net MWF. The equivalent sea level change (ESL) calculated from GLAC-1D is shown in Fig. 2.1. To account for iceberg meltwater associated with ice-sheet calving, GLAC-1D additionally provides the calving flux of the Northern Hemisphere ice sheets (Fig. 2.2). The main contribution to the global signal is the meltwater discharge in the North Atlantic/Arctic catchment area. Because of the lack of an explicit iceberg model, we impose the calving part into the ice-rafted debris (IRD) belt (40°N–55°N, 45°W–20°W; Hemming, 2004) of the North Atlantic. Given that temporal change in ice volume consists of both ice melting and calving, meltwater that drains along the coastline is derived from the residual ice volume change which excludes the calving part. This kind of freshwater flux is defined as

$$MWF = MWF_{coastal} + MWF_{calving} \tag{2.1}$$

$$MWF_{coastal} = MWF * \frac{\sum MWF - \sum MWF_{calving}}{\sum MWF} \tag{2.2}$$

where MWF is total freshwater flux calculated from the temporal derivative of ice thickness, $MWF_{coastal}$ is the meltwater part which is distributed in the coastal area, $MWF_{calving}$ is the calving fraction of discharge from Northern Hemisphere ice sheets which is distributed into the IRD belt, $\sum MWF$ and $\sum MWF_{calving}$ represent the sum of total freshwater and the calving fraction, respectively. In the following, the notation MWF refers to the combined flux associated with melting and calving to represent the analogue contribution to meltwater perturbations in hosing experiments. Please note that this does not mean that our model approach ignores precipitation minus evaporation which is inherently represented by the hydrological cycle within COSMOS.

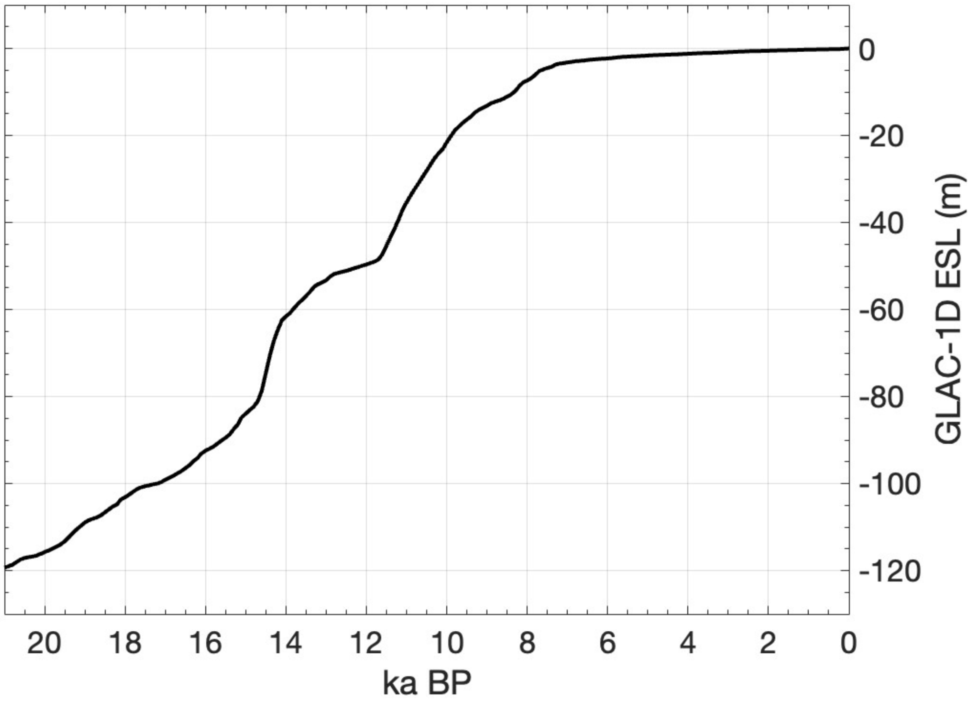

Fig. 2.1 Time evolution of the equivalent sea level change (ESL) calculated from GLAC-1D.

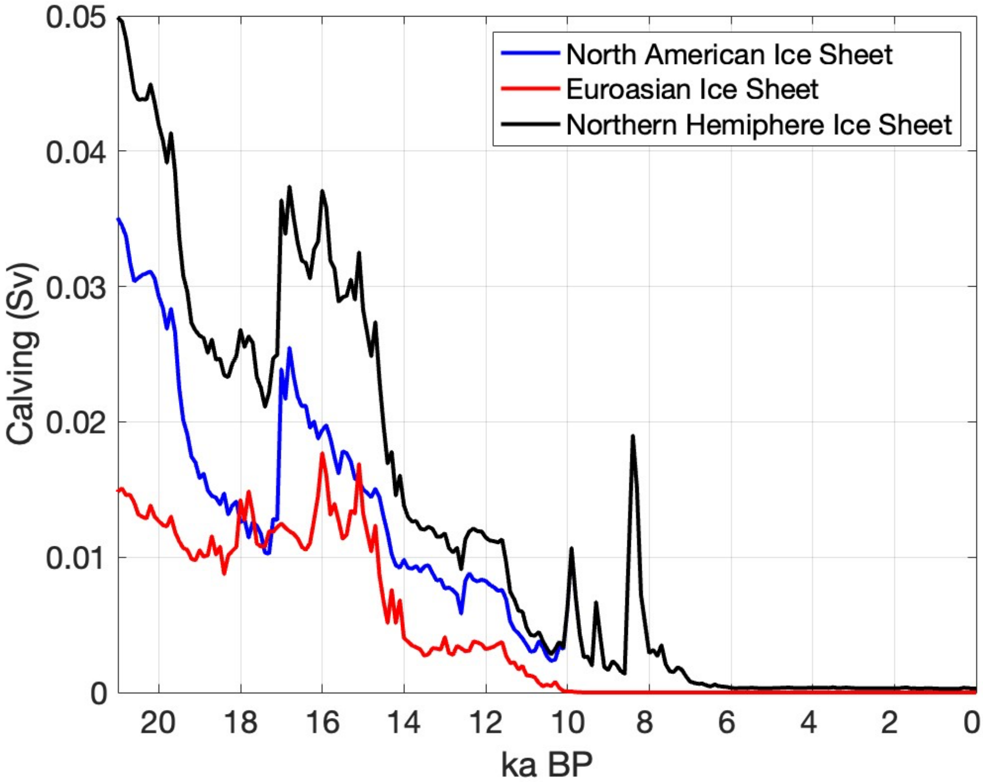

Fig. 2.2 Time evolution of the calving fraction in GLAC-1D.

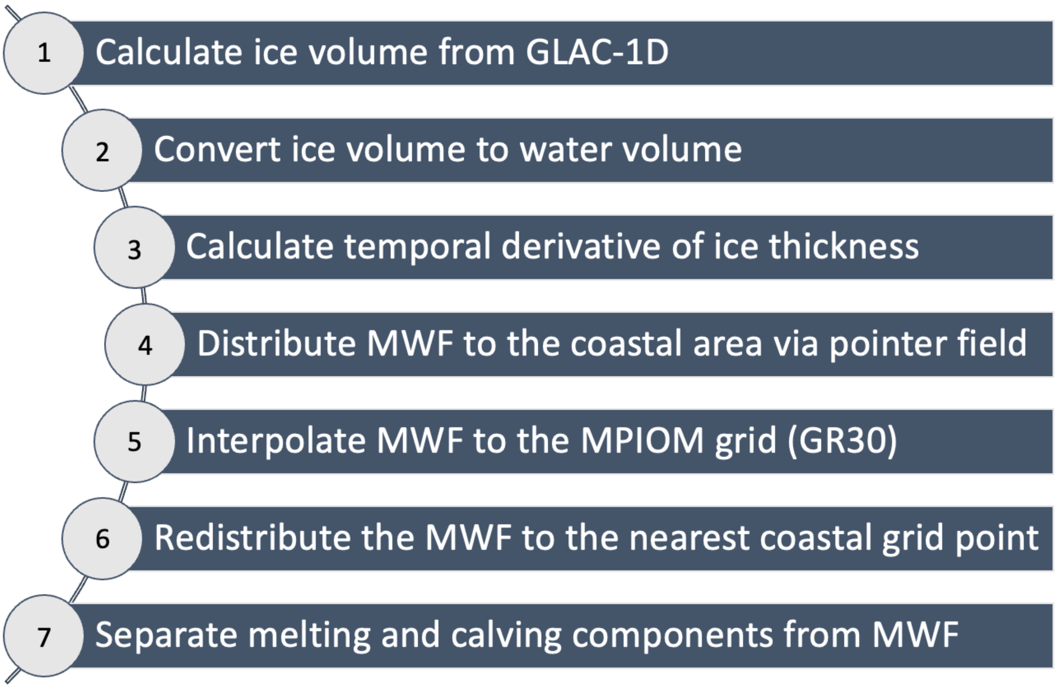
1 Calculate ice volume from GLAC-1D
2 Convert ice volume to water volume
3 Calculate temporal derivative of ice thickness
4 Distribute MWF to the coastal area via pointer field
5 Interpolate MWF to the MPIOM grid (GR30)
6 Redistribute the MWF to the nearest coastal grid point
7 Separate melting and calving components from MWF

Fig. 2.3 Flow chart for the means calculating MWF in GLAC-1D

2.3 Model setup for the transient simulation

For the deglacial transient experiments in this study, the model was integrated from a glacial state at 16 ka towards B/A following the protocol of PMIP4 (Ivanovic et al., 2016). The orbital forcing is from Berger (1978) and the atmospheric greenhouse gas concentrations are prescribed according to reconstructions from ice cores (Bereiter et al., 2015; Loulergue et al, 2008; Schilt et al., 2010; Köhler et al., 2017). As introduced in section 2.2, Ice sheets and surface topographies were prescribed from GLAC-1D. To ensure the comparability of the experiments done in this study for the last deglaciation with other COSMOS experiments, we did not take the topography from GLAC-1D directly, but applied the differences between each time slot in GLAC-1D and its PI to the topography of one PI experiment, which has been run into equilibrium over several thousand years (Wei et al., 2012; Zhang et al., 2013). Since the horizontal resolution of GLAC-1D is 0.5 degrees, it is far better than the resolution in our model. Therefore, we apply the orography data of GLAC-1D to the Subgrid Scale Orographic Parameterization (SSOP) scheme in the ECHAM5 model to represent the effects of orographic variations on smaller scales (Lott & Miller, 1997; Lott, 1999). The orography may affect the atmospheric flow in many ways. The SSOP can help ECHAM5 take into account the momentum transfer from the earth to the atmosphere accomplished by orographic gravity waves and the drag exerted by the subgrid scale mountains when the air flow is blocked at low levels.

During the deglaciation, the melting of the ice sheets not only changed the topography and thus dynamically altered the atmospheric circulation, but the change in the area covered by the ice also changes the surface albedo and thus thermally affects the climate. We therefore applied the glacier information from GLAC-1D to ECHAM5 and JSBACH as a way to consider the effect of ice cover extent changes on albedo. For grid points newly covered by ice, the background albedo at that location is modified to the level of the ice cover, which is 0.7 in our simulations; while for grid points where the land below is exposed to the air due to ice sheet retreat, the land type and vegetation information at that location is supplemented by data from the PI period.

Due to the limitations of the temporal resolution in the GLAC-1D datasets, the forcing fields associated with the ice sheet change (orography, freshwater, and surface albedo) were updated every hundred model years. Other forcings (orbital parameters and greenhouse gases) were updated every model year.

Chapter 3 Ice sheet decline and rising atmospheric CO_2 control AMOC sensitivity to deglacial meltwater discharge

The last deglaciation was characterized by a sequence of abrupt climate events thought to be linked to rapid changes in Atlantic meridional overturning circulation (AMOC). The sequence includes a weakening of the AMOC after the Last Glacial Maximum (LGM) during Heinrich Stadial 1 (HS1), which ends with an abrupt AMOC amplification at the transition to the Boelling/Alleroed (B/A). This transition occurs despite persistent deglacial meltwater fluxes that counteract vigorous North Atlantic deep-water formation.

In this chapter, we investigate changes in the AMOC with respect to key forcings and boundary conditions during deglaciation including changes in atmospheric CO_2 concentration and continental ice sheets by a suite of simulations with the fully-coupled ocean-atmosphere-sea ice-land surface model COSMOS. Ice Sheet changes include associated deglacial meltwater and iceberg fluxes based on the state-of-the art GLAC-1D reconstruction (Tarasov et al. 2012). In particular we show that the decline of Northern Hemisphere ice sheets increases the sensitivity of the AMOC to North Atlantic meltwater discharge while rising atmospheric CO_2 concentrations tend to counteract this effect. Therefore, the climate system, as represented by COSMOS, can to first order undergo HS1 to B/A transition without changes in surface meltwater routing nor changes in the net meltwater discharge from the ice sheets.

3.1 Experimental design

In the following section we describe the experimental set-up of the model simulations that represent the basis for this study. An overview of experiment characteristics is provided in Table 3.1. Details of the prescribed GLAC-1D orography and deglacial meltwater discharge fields are provided in Table 3.1 and Figs. 3.1-3.3

Table 3.1: Summary of experimental design details of all simulations in this chapter.

ID	Boundary Conditions	Initial Conditions	Freshwater Routing	Global Meltwater Magnitude	Atlantic/ Arctic Melting	Atlantic/ Arctic Calving	Integration of Model Years
16KCTL	16 ka	LGM		0Sv	0Sv	0Sv	1000
16K_0.05	16 ka	LGM	MWF1	0.054Sv	0.004Sv	0.036Sv	1200
16K_0.10	16 ka	LGM	MWF2	0.101Sv	0.046Sv	0.026Sv	1650
16K_0.15	16 ka	LGM	MWF3	0.151Sv	0.095Sv	0.030Sv	2200
16K_0.21	16 ka	LGM	MWF4	0.208Sv	0.154Sv	0.031Sv	3500
16K_0.1_0.2_grad	16 ka	16K_0.10	MWF2	0.101Sv to 0.208Sv	0.046Sv to 0.095Sv	0.026Sv to 0.054Sv	1000
16K_0.21_CO2	16 ka, transient CO_2	model year 2000 in 16K_0.21	MWF4	0.208Sv	0.154Sv	0.031Sv	1400
LGM_16KICE	16ka ice sheet, LGM CO_2, LGM ORB	LGM		0Sv	0Sv	0Sv	800
LGM_16KICE+0.10	16ka ice sheet, LGM CO_2, LGM ORB	LGM_16KICE	MWF2	0.101Sv	0.046Sv	0.026Sv	800
LGM_16KICE+0.15	16ka ice sheet, LGM CO_2, LGM ORB	LGM_16KICE	MWF2	0.151Sv	0.069Sv	0.039Sv	800
LGM_0.10	LGM	LGM	MWF2	0.101Sv	0.046Sv	0.026Sv	800
LGM_0.18	LGM	LGM	MWF2	0.180Sv	0.082Sv	0.046Sv	800
16KCTL_0.21	16 ka	16KCTL	MWF4	0.208Sv	0.154Sv	0.031Sv	400

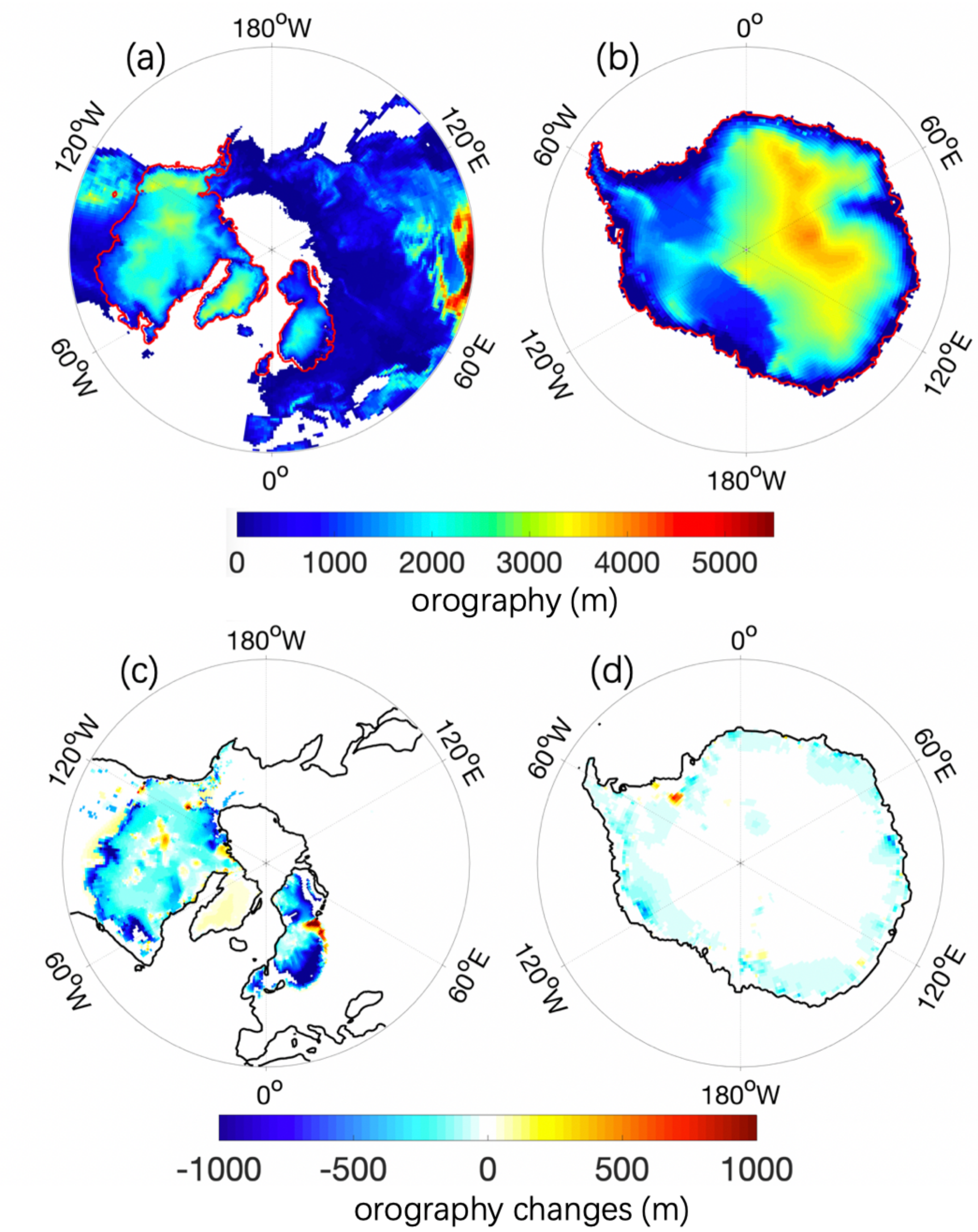
(a)
180°W
120°W
120°E
60°W
60°E
0°
(b)
0°
60°W
60°E
120°W
120°E
180°W
0
1000
2000
3000
4000
5000
orography (m)
(c)
180°W
120°W
120°E
60°W
60°E
0°
(d)
0°
60°W
60°E
120°W
120°E
180°W
-1000
-500
0
500
1000
orography changes (m)

Fig. 3.1 Orography (m) at 16 ka from GLAC-1D in **a)** the Northern Hemisphere and **b)** the Southern Hemisphere. The ice sheet extent is indicated by red lines. In panels **c)** and **d)** the orography anomalies between LGM and 16 ka are shown. The black lines in panels **c)** and **d)** represent the coastline at the LGM.

3.1.1 Equilibrium HS1 experiments

Geological evidence suggests the occurrence of meltwater pulses at 19 ka B.P. (19 ka MWP) (Clark et al., 2004), 17.5 ka and 16 ka (Bard et al., 2000). Before we perform any experiments with meltwater fluxes, a simulation without meltwater input is conducted as the control state for 16 ka conditions in experiment 16KCTL. The orbital forcing is from Berger (1978) and the atmospheric greenhouse gas concentrations are prescribed according to reconstructions from ice cores (Bereiter et al., 2015; Loulergue et al, 2008; Schilt et al., 2010; Köhler et al., 2017). This simulation is initialized from an LGM simulation, which has been integrated for 4000 years under PMIP3 LGM background conditions (Zhang et al. 2013) representative of climate state at 21 ka. The orbital parameters and Greenhouse Gas (GHG) at 16ka and LGM are listed in Table 3.2. Based on the 16ka state we designed a suite of sensitivity experiments to test the impact of different meltwater fluxes on AMOC. The Bering St. is closed in all simulations.

According to GLAC-1D, for time interval from 16 ka to B/A onset (i.e., 14.6ka), the total amount of global net meltwater flux spans a range between 0.04Sv and 0.21Sv. To assess the potential AMOC changes to a range of meltwater variations in the corresponding time interval, (as well as partially address GLAC-1D chronological uncertainties) we chose four different meltwater discharge configurations (Table 3.1, Figs. 3.2, 3.3) representative of freshwater forcing at 16 ka (MWF1 in experiment 16K_0.05 with 0.05 Sv), 14.9 ka (MWF2 in experiment 16K_0.1 with 0.10 Sv), 15.4 ka (MWF3 in experiment 16K_0.15 with 0.15 Sv) and 15.2 ka (MWF4 in experiment 16K_0.2 with 0.21 Sv). Additionally, we performed one experiment (16K_0.1_0.2_grad) with a gradual MWF increase from 0.1Sv to 0.21 Sv in 1000 years based on 16K_0.1.

We note that in the scenario without freshwater forcing, AMOC is in a phase of gradual enhancement on its own within the first 500 model years after switching the boundary condition from LGM to 16 ka

(16KCTL in Fig. 3.5). As for the freshwater sensitivity experiments, the system needs to respond to freshwater forcing while adjusting from the LGM boundary conditions to 16 ka. Therefore, whether the system will respond nonlinearly to the freshwater forcing and thus alter the results during the spin-up phase of the 16-ka freshwater experiment is an issue we need to consider. To test the potential synergetic effects that might arise from applying the forcings at the same time, we have performed an additional experiment and started the meltwater flux of 0.21 Sv (MWF4) at year 500 in 16KCTL, which is aligned to year zero in the Fig. 3.5. In Fig. 3.4 we can see that the resulting AMOC trajectory is similar in both experiments 16K_0.21 and 16CTL_0.21. This suggests that the timing of the application of freshwater forcing does not fundamentally affect the results.

Table 3.2 Orbital parameters and GHGs in 16ka and LGM

		16 ka	**LGM**
Orbital Parameters	eccentricity	0.019626	0.018994
	obliquity	23.750	22.949
	Perihelion-180°	197.229	114.42
GHGs	CO_2	221.71 ppm	185 ppm
	CH_4	458.59 ppb	350 ppb
	N_2O	205.76 ppb	200 ppb

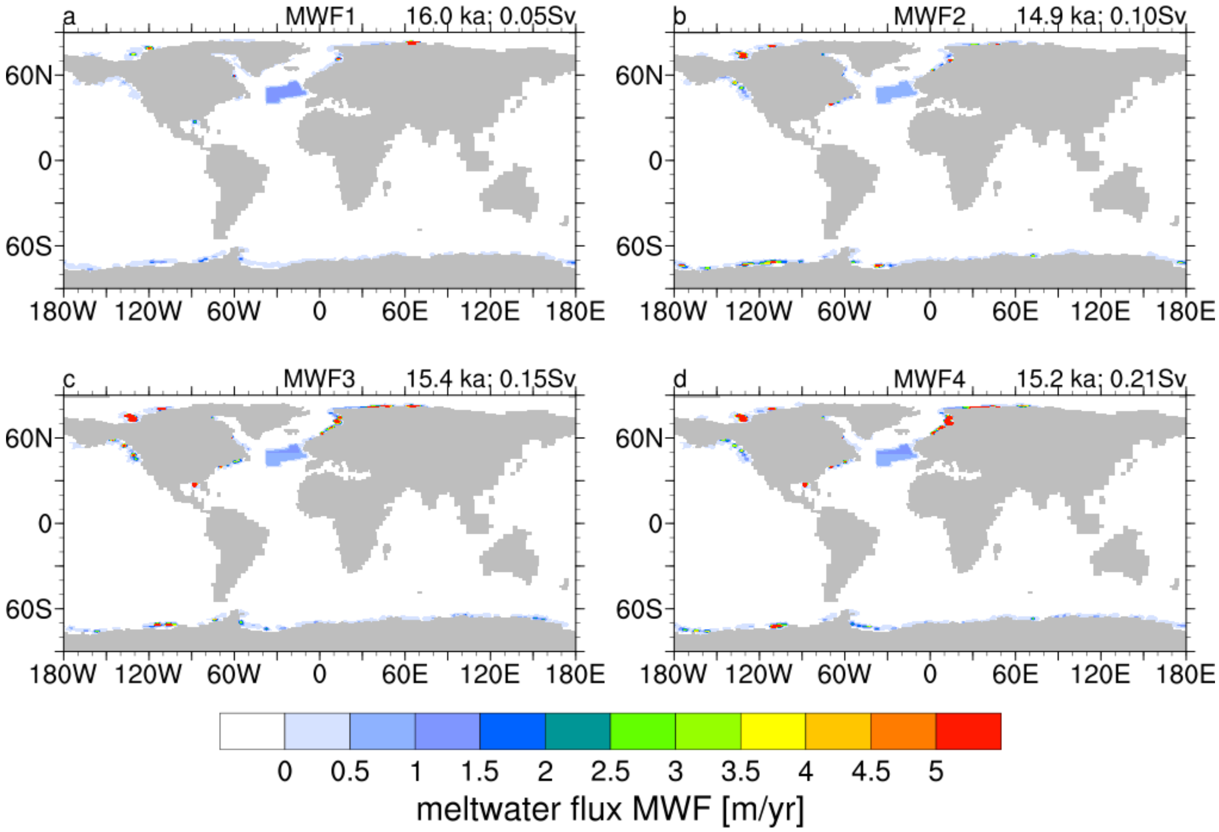
a
MWF1
16.0 ka; 0.05Sv
b
MWF2
14.9 ka; 0.10Sv
c
MWF3
15.4 ka; 0.15Sv
d
MWF4
15.2 ka; 0.21Sv
60N
0
60S
180W
120W
60W
0
60E
120E
180E
0
0.5
1
1.5
2
2.5
3
3.5
4
4.5
5
meltwater flux MWF [m/yr]

Fig. 3.2 Map of meltwater discharge (meltwater flux in m/yr) in the different simulations at a) 16 ka, b) 15.4 ka, c) 15.2 ka, d) 14.9 ka. The meltwater forcing fields consist of two parts: the melt water part of the glacial ice sheets (located at different coastal regions) and the part due to iceberg melting in the IRD belt of the North Atlantic. The MWF is derived from the GLAC-1D reconstruction.

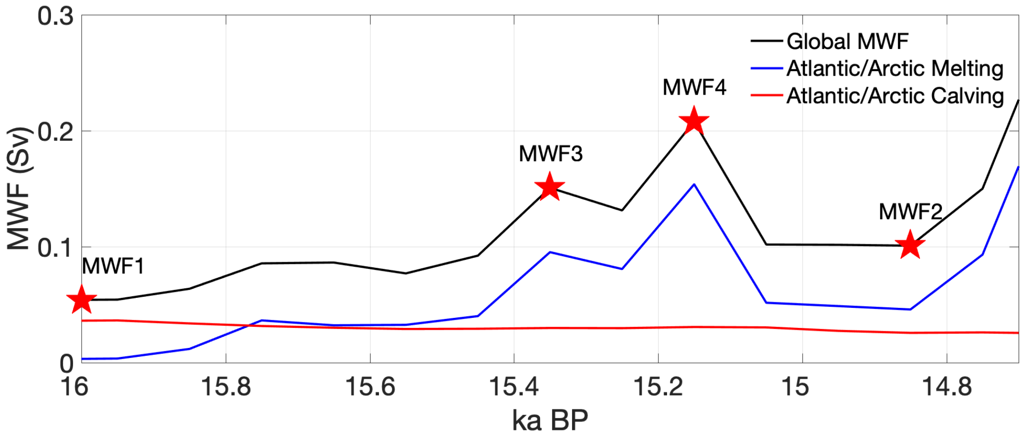

Fig. 3.3 Temporal evolution of the total global (black) meltwater flux (Sv) and the Atlantic contributions by melting (blue) and calving (red) from

GLAC-1D between 16ka and 14.6ka. The red stars correspond to the MWF scenarios 1 to 4 in Fig. 3.2 and Table 3. 1.

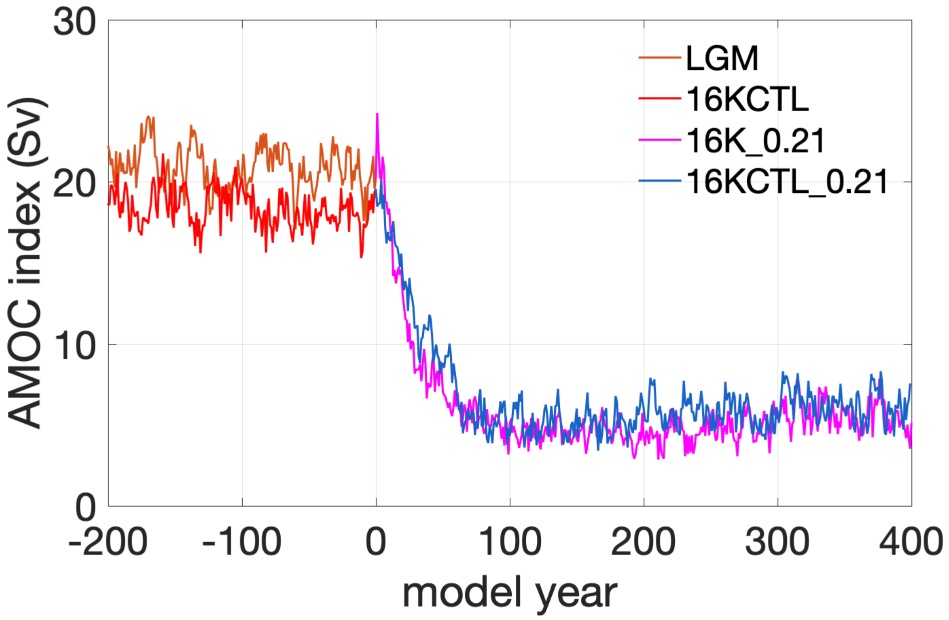

Fig. 3.4 Time evolution of the AMOC (Sv) defined as the maximum value of the stream function below 500 m in the North Atlantic for different sensitivity experiments (cf. Figs. 3.2, 3.3, 3.5 and Table 3.1). The 16KCTL shown here is intercepted from the results in Fig. 3.5 for the model years 300 to 500.

3.1.2 Ice sheet and atmospheric CO_2 sensitivity experiments

For comparison with the 16 ka state experiments, we conducted two LGM state hosing experiments that apply the deglacial meltwater discharge pattern according to MWF2 in experiments LGM_0.1 and LGM_0.18. The respective discharge magnitudes in these two LGM experiments are 0.1 Sv and 0.18 Sv, respectively (cf. section 3.2.3).

The 16 ka and LGM simulations are complemented by three experiments with hybrid boundary conditions that all represent full LGM conditions except a 16-ka ice sheet configuration to disentangle CO_2 and ice-sheet effects. Experiment LGM_16KICE is conducted without any meltwater discharge resulting from to ice volume changes. In contrast ice volume changes equivalent to a meltwater flux of 0.1 Sv and 0.15 Sv are distributed by the MWF2 pattern in experiment LGM_16KICE+0.1 and LGM_16KICE+0.15, respectively.

The HS1-B/A transition occurred around 14.7 ka. According to GLAC-1D, the total amount of meltwater flux at this time is ~0.22 Sv, which is larger than that used in our freshwater sensitivity runs. Depending on the geographic pattern of injection, such a large amount of freshwater could force the AMOC into a weak mode. To return to a strong AMOC mode, other forcing might have played a key role, such as a gradual CO_2 increase (Zhang et al., 2017). Therefore, we test whether a rise in atmospheric CO_2 concentration might restore the AMOC in the presence of a large amount of freshwater flux. Among our freshwater sensitivity experiments, the experiment MWF4 has the largest freshwater input (0.21 Sv), which is close to the amount of freshwater when the BA event occurs in the GLAC-1D reconstruction. A transient experiment (16K_0.21_CO2) mimicking the CO_2 rise into the B/A is conducted to test the CO_2 effect for the AMOC recovery process with the presence of this large MWF.

3.2 Results

The application of the various boundary conditions (Table 3.1, Figs. 3.1-3.3) reveals three basic types of AMOC trajectories (Fig. 3.5). The first is a modest AMOC weakening, which occurs in experiments LGM_16KICE and 16KCTL. The second is a relatively strong transient AMOC reduction followed by an abrupt AMOC intensification after several hundreds of years under fixed deglacial MWF in experiments 16K_0.05, 16K_0.1, 16K_0.15. The third trajectory is simulated in experiment 16K_0.21, which shows a persistent weak AMOC without a rapid AMOC recovery. In Fig. 3.5 we show AMOC states in the different experiments, which are obtained by averaging over the last 100 model years of each individual simulation in Fig. 3.5. All states are characterized by weaker Atlantic overturning than in the LGM control state.

In our 16-ka control simulation (16KCTL) the AMOC stabilizes at ~18 Sv, which is slightly weaker than the LGM state at ~21 Sv. If we fix the atmospheric CO_2 concentration and the orbital forcing at the level of the LGM state, and only change ice-sheet configuration to that at 16ka (LGM_16KICE), the AMOC change is very similar to 16KCTL. This suggests that the decrease in ice-sheet height is the main cause of the reduced AMOC in 16KCTL and shows that without any additional forcing (e.g., MWF) 16 ka boundary conditions are not sufficient to give rise to evident AMOC decrease as suggested by reconstructions (e.g., McManus 2004). To address the differences that govern the transient AMOC dynamics in the hosing experiments we investigate the mechanism for an abrupt AMOC intensification in section 3.2.1. Thereafter in section 3.2.2, we focus on the impact of rising CO_2 on the threshold for the rapid AMOC amplification. In section 3.2.3 we examine the effect of terrestrial ice decline on the AMOC sensitivity to deglacial meltwater flux.

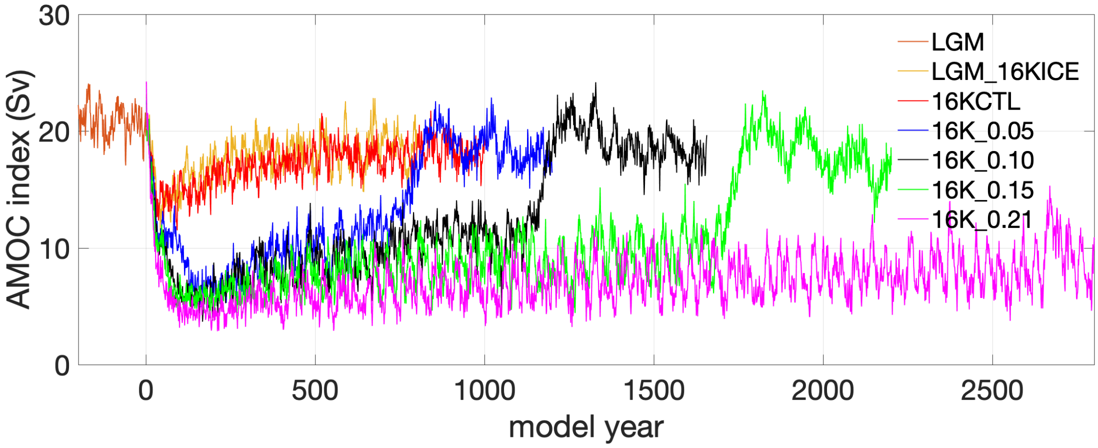

Fig. 3.5 Time evolution of the AMOC (Sv) defined as the maximum value of the stream function below 500 m in the North Atlantic for different

sensitivity experiments (cf. Figs. 3.2, 3.3 and Table 3.1).

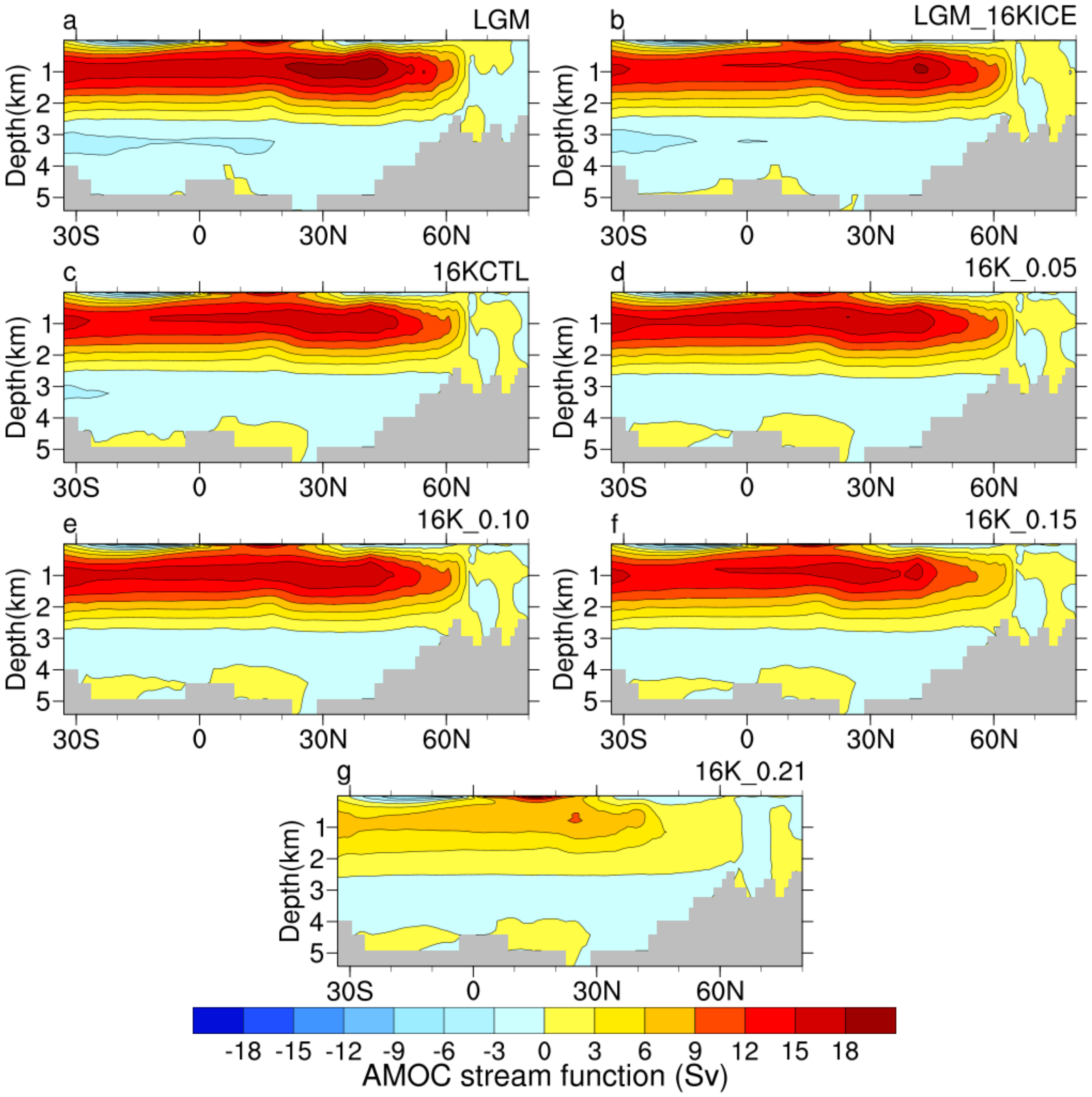

Fig. 3.6 AMOC (Sv) for the sensitivity experiments in Fig. 3.5, represented by the average of the last 100 model years. Positive and negative values indicate clockwise and anti-clockwise circulation, respectively.

3.2.1 Mechanism of AMOC recovery

In the three hosing experiments 16K_0.05, 16K_0.10, and 16K_0.15, the AMOC shifts from its weak to strong mode (Fig. 3.5). The duration of the weak AMOC phase is longer for a stronger MWF and an abrupt amplification process takes place after more than 1500 years in experiment 16K_0.15, which has the strongest sub-critical MWF for the rapid AMOC amplification. All three experiments have an extended phase of gradual AMOC increase prior to the abrupt transition in common. Fig. 3.7 shows the composite trend analysis of different variables in the gradual phase of these experiments. Over the sea surface, a background warming (~1 °C ka^{-1}) decreases the surface water density in the northeastern North Atlantic (NENA, the main convection sites) (Fig. 3.7c). This strengthens the vertical stratification thermally and stabilizes a weak AMOC. However, at the same time the local sea surface salinity (SSS) has an increasing trend of 0.07 psu ka^{-1}, which counteracts the thermal effect and increases the surface water density (0.5 kg m^{3} ka^{-1}) (Fig. 3.7d, e). Similarly, density in the subsurface layer also increases, but with a slower trend than the surface (Fig. 3.7e inset). This vertical contrast in the rate of water density change highlights the importance of a de-stratification via surface salinization. Especially the simulated southward-shifted Intertropical Convergence Zone (ITCZ) during the initial AMOC weakening during the first 200 years of hosing are instrumental to increase salinity in the western subtropical North Atlantic (WSNA, 60 –90° W, 10 –30° N) by an increased moisture transport across Central America (Zhang et al., 2017). Since the AMOC is not completely stagnant, the salty WSNA water masses are transported northwards to the North Atlantic deep-water formation areas. This increases the SSS in the northern NA, counteracting the freshwater flux and hence promoting an initial AMOC strengthening once the AMOC reaches its weak mode. As a result, enhanced vertical mixing is identified along the extension area of the Gulf Stream, which leads to a local sea surface warming and an increase in sea surface salinity (Fig. 3.7c, d) by stronger evaporation. This further increases the vertical mixing and the strength of AMOC providing positive feedback, which is key to explain the AMOC recovery in our MWF experiments. Taking experiment 16K_0.1 as an example (Fig. 3.8), salinity is rising in the upper 2000 m of the water column in the North Atlantic, with the most pronounced salinity increase at the surface (Fig. 3.8a).

In order to estimate the relative importance of the northward salinity transport relative to changes in the AMOC strength, the freshwater transported by the upper branch of AMOC in the Atlantic Ocean is calculated for different model years. For a quantitative analysis, this transport is defined as

$$MFT = \int_{-h}^{0} \left(\frac{S_{ref} - \bar{S}}{S_{ref}}\right) \bar{v} dz, \qquad (3.1)$$

where h is the bottom depth of the upper branch of AMOC, S_{ref} is a reference salinity (mean salinity of the Atlantic Ocean), and $\bar{S}$ and $\bar{v}$ denote zonally averaged salinity and integrated northward velocity, respectively (cf. Lohmann, 2003). By calculating the meridional freshwater transport (MFT), it can be seen that northward salinity across 43°N (i.e., the latitude between Gulf Stream extension and sea ice cover) is rising along with the AMOC strengthening until the AMOC amplifies to the strong mode (Fig. 3.8b).

During the abrupt recovery phase, the preceding ~600yr phase of gradual warming (Fig. 3.8c) at water depths below ~1500 m plays an important role. As AMOC weakens, a reduced vertical mixing slows down the heat exchange between the cold sea surface and warmer subsurface, leading to a gradual heat accumulation with a maximum temperature increase at ~2000 m. This warming effect on density is not strong enough to overcome the in-situ freshening at the sea surface to generate a destabilization of the stratification. However, when the warm water masses are ventilated to the sea surface, they promote the surface warming, sea-ice retreat and vertical mixing. Given that the core of this warming is at ~2000m water depth, this positive feedback works only when the strength of the AMOC reach a certain level that enable the water masses to be ventilated to the surface. Hence, this becomes particularly important positive feedback once the AMOC transition has started (Fig. 3.8d).

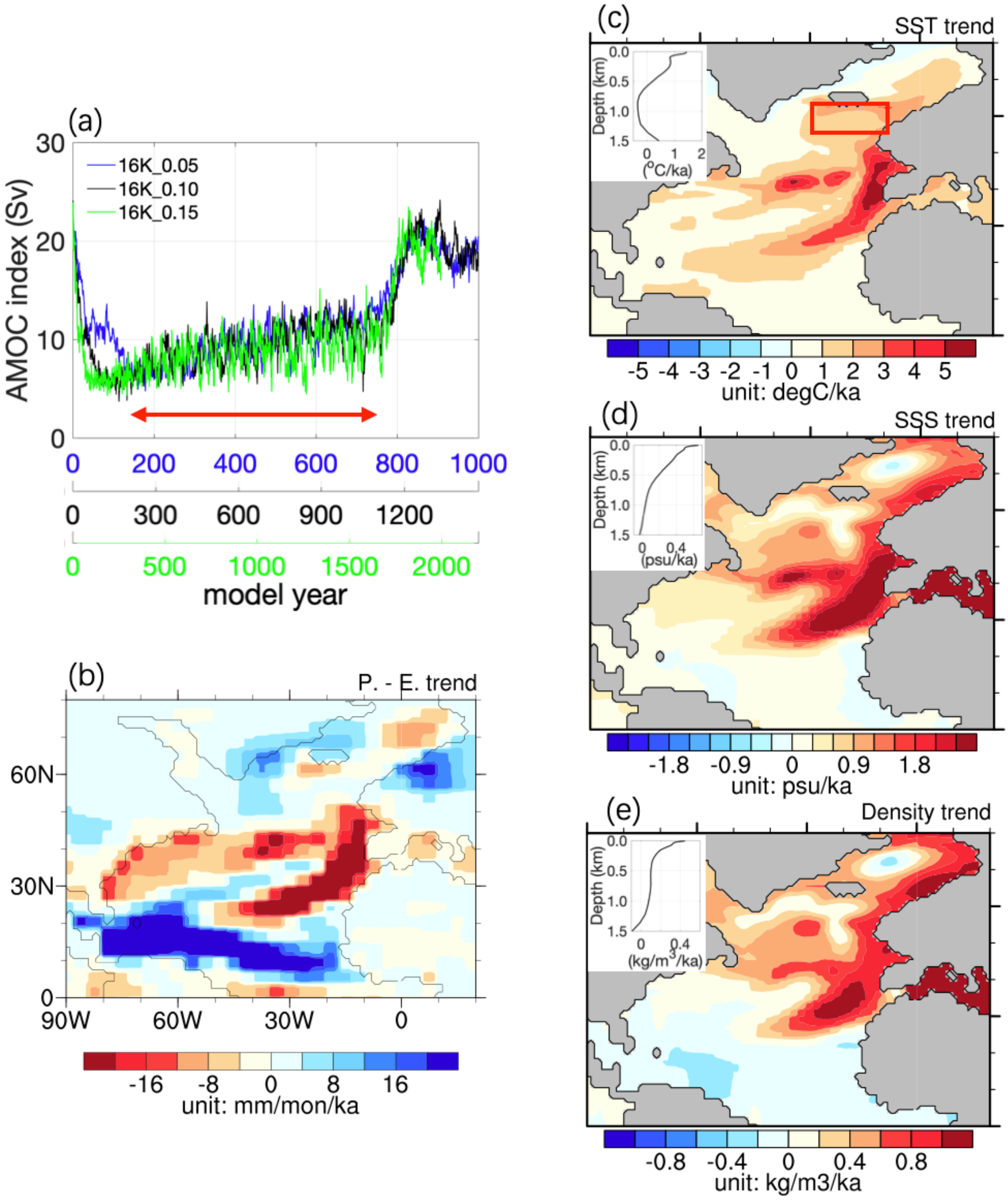

Fig. 3.7 Trend evolution in the three 16-ka experiments with a transient weakening of the AMOC. **a)** Time scales of AMOC index (Sv) on the corresponding experiment. The arrow marks the period which is used to calculate the composite trend in **b)** to **e)**. **b)** precipitation minus evaporation (mm mon^{-1} ka^{-1}), **c)** sea surface temperature (SST, °C ka^{-1}), **d)** sea surface salinity (SSS, psu ka^{-1}) and **e)** sea surface density (kg m^{-3} ka^{-1}). **c)** to **e)** contain an inlet plot for the vertical profiles over the index region NENA as defined by the red rectangle in panel **c)**.

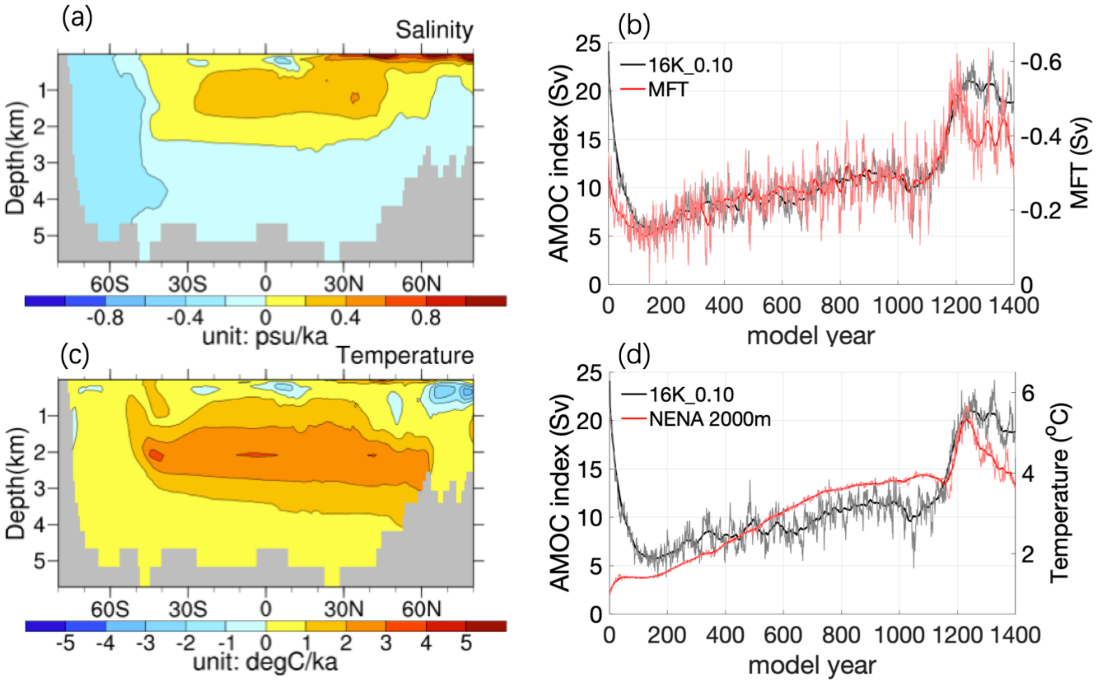

Fig. 3.8 Trend evolution in experiment 16K_0.1 between model year 200 to 1100. Zonal mean trends in the Atlantic Ocean for **a)** salinity (psu ka^{-1}) and **b)** temperature (°C ka^{-1}). **c)** Time evolution of AMOC index (Sv, black) and MFT in the upper AMOC brunch at 43°N (Sv, red). **d)** The subsurface (2000m) temperature (°C, red) evolution averaged in the NENA area. Bold lines in **b)** and **d)** represent 50 yr running-mean values.

3.2.2 CO_2 effect on AMOC recovery threshold

From 16 ka to the onset of the B/A, the maximum MWF is 0.21 Sv at 15.2 ka. As shown in Fig. 3.5, this amount of MWF is so strong that the AMOC remains in the weak mode throughout simulation 16K_0.21. In experiment 16K_0.21_CO2 we apply a gradual CO_2 increase, from 222ppm to 241ppm in 300 years based on simulation 16K_0.21 to test whether a CO_2 rise can trigger the deglacial AMOC recovery. As shown in Fig. 3.9, an abrupt transition takes place ~1000 years after CO_2 starts to rise. During the gradual phase prior to the abrupt AMOC recovery changes in the MFT across 43°N are similar in both experiments (Fig. 3.10a). However, the simulated temperature trends in NENA reveal fundamental differences (Fig. 3.10b). Notably, the temperature trend is positive at all depth levels in in our CO_2 experiment 16K_0.21_CO2. In contrast the upper ~800 m in our fixed CO_2 experiment 16K_0.21 are characterized by a cooling trend. Furthermore, subsurface temperatures below ~200 m in 16K_0.21_CO2 show a stronger trend throughout all depth levels of the weakened NADW-cell. The resulting sub-surface warming in the northern North Atlantic (Fig. 3.10c) leads to an increasing temperature inversion as a key driver of vertical water mass destratification in NENA.

Approximately 1000 years after the start of the CO_2 rise in experiment 16K_0.21_CO2 the stratification at the convection sites breaks down, and the AMOC recovers. From the difference in surface salinity in the last 100 years of the two experiments (Fig. 3.10d), it can be seen that after the recovery of the AMOC in the 16K_0.21_CO2 experiment, the SSS in the North Atlantic is larger than in the same interval of the 16K_0.21 experiment. The difference is concentrated at the Gulf Stream extension area and North-Eastern Atlantic. Although the timing of a specific meltwater chronology relative to the CO_2 increase might be different, the comparison of the two experiments clearly reveals that a weak AMOC is more likely to recover from HS1 for a higher atmospheric CO_2 concentration.

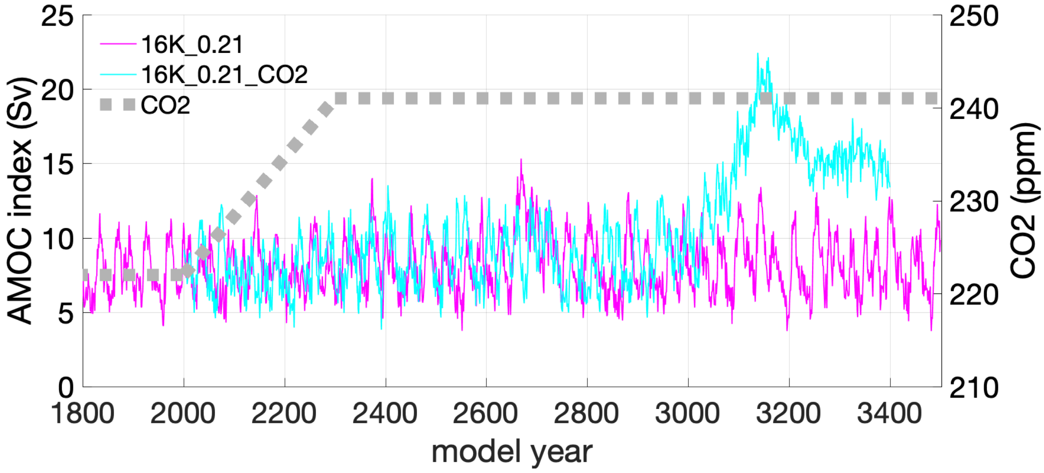

Fig. 3.9 Time evolution of the AMOC index (Sv) for experiments 16K_0.21

and 16K_0.21_CO2 in response to prescribed atmospheric CO_2 changes (dashed grey line). CO_2 gradually increases from 222 to 241ppm in the first 300 years in 16K_0.21_CO2. Experiment 16K_0.21_CO2 starts from model year 2000 of 16K_0.21.

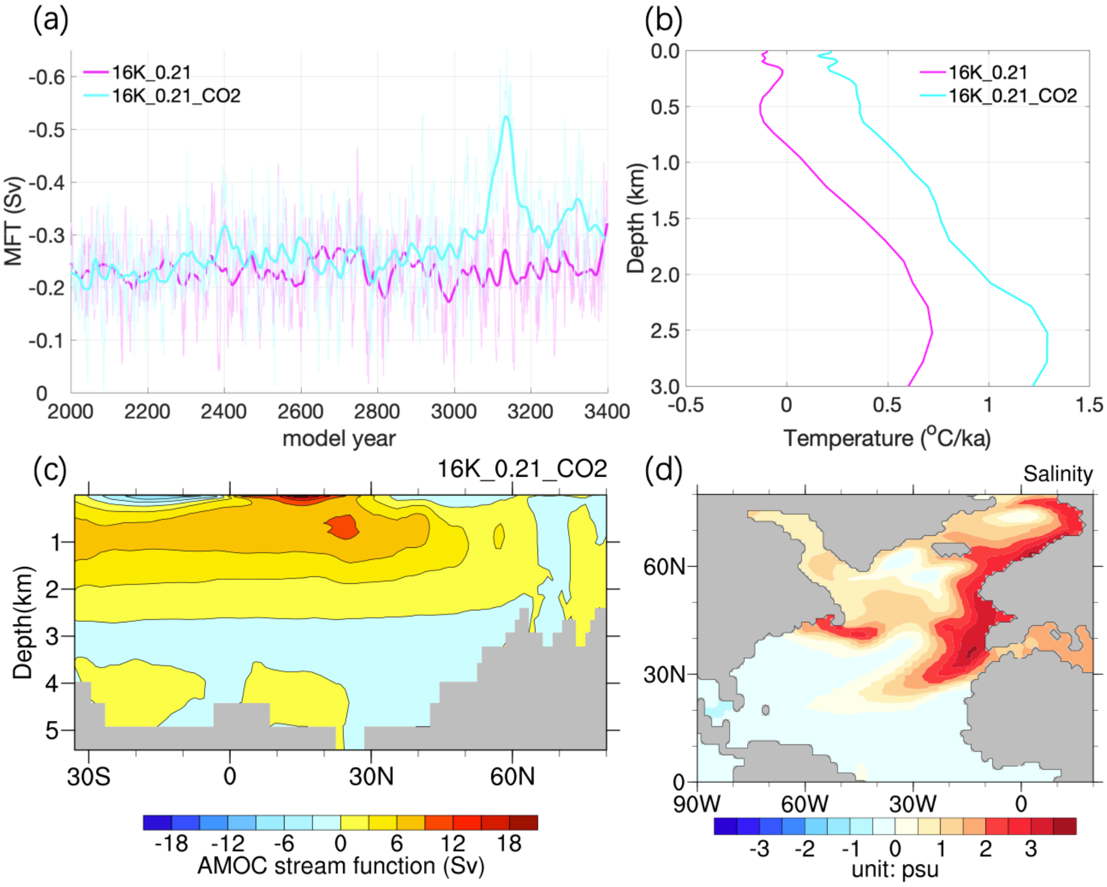

Fig. 3.10 Experiment characteristics in 16K_0.21 and 16K_0.21_CO2. **a)** Time evolution of the MFT in the upper brunch of the AMOC at 43°N (Sv), **b)** vertical temperature profile trends, **c)** Atlantic stream function in 16K_0.21_CO2 averaged between 2800 and 2900 model years, **d)** SSS (psu) difference (16K_0.21_CO2 minus 16K_0.21) averaged between model years 3300-3400. Bold solid lines in **a)** are 50 yr running mean values.

3.2.3 Ice Sheet changes and AMOC meltwater sensitivity

So far, we found that the deglacial ice decline generates an AMOC weakening and that under the influence of deglacial meltwater in experiment 16K_0.21 the AMOC resides in a weaker state without any sign of an abrupt AMOC amplification, unless atmospheric CO_2 increases to B/A levels.

We perform experiment 16K_0.1_0.2_grad to narrow the range in which meltwater flux threshold for abrupt AMOC change is. In this experiment, based on simulation 16K_0.1 we gradually increase the meltwater flux from 0.1 to 0.2 Sv in 1000 years (Fig. 3.11a). Experiment 16K_0.1_0.2_grad shows that the AMOC strong-to-weak transition occurred once fluxes are greater than ~0.17 Sv under full 16 ka conditions. Accordingly, we further test how ice sheet changes influence on the AMOC sensitivity. In experiment LGM_0.18 we apply a MWF larger than the detected threshold under 16 ka conditions, but for full LGM conditions. This experiment shows that the resulting AMOC is stronger (Fig. 3.11b) than under 16 ka conditions with the same MWF (Fig. 3.11a), revealing a less sensitive LGM AMOC. Together with our knowledge from the previous section that rising CO_2 can transform a super-critical (16K_0.21) to a sub-critical (the end of 16K_0.21_CO2) MWF perturbation, this result tends to indicate that a larger ice sheet results in a less sensitive AMOC to meltwater fluxes. To further pinpoint the role of declining ice sheets in this sensitivity modulation we perform experiment LGM_16KICE+0.15. In this experiment only the 16-ka ice sheet configuration replaces LGM ice sheet conditions and a MWF of 0.15 Sv is applied (i.e., smaller than the threshold value under 16 ka conditions). This experiment reveals a relatively high sensitivity to deglacial meltwater flux with an AMOC weakening of ~10 Sv (Fig. 3.11b). The reduction and the resulting AMOC (Fig. 3.11c) largely resemble the characteristics in experiment 16K_0.21 (Figs. 3.5 and 3.6g) in spite of the weaker meltwater forcing in LGM_16KICE+0.15. The higher AMOC sensitivity is linked to changes in the westerlies and zonal wind stress (cf. Zhang et al., 2014) that favors enhanced sea ice export to the northeastern North Atlantic. This causes weaker open ocean ventilation and a weaker NADW-cell in experiment LGM_16KICE than in the LGM simulation (Fig. 3.6a, b) and LGM_16KICE being more susceptible to meltwater flux.

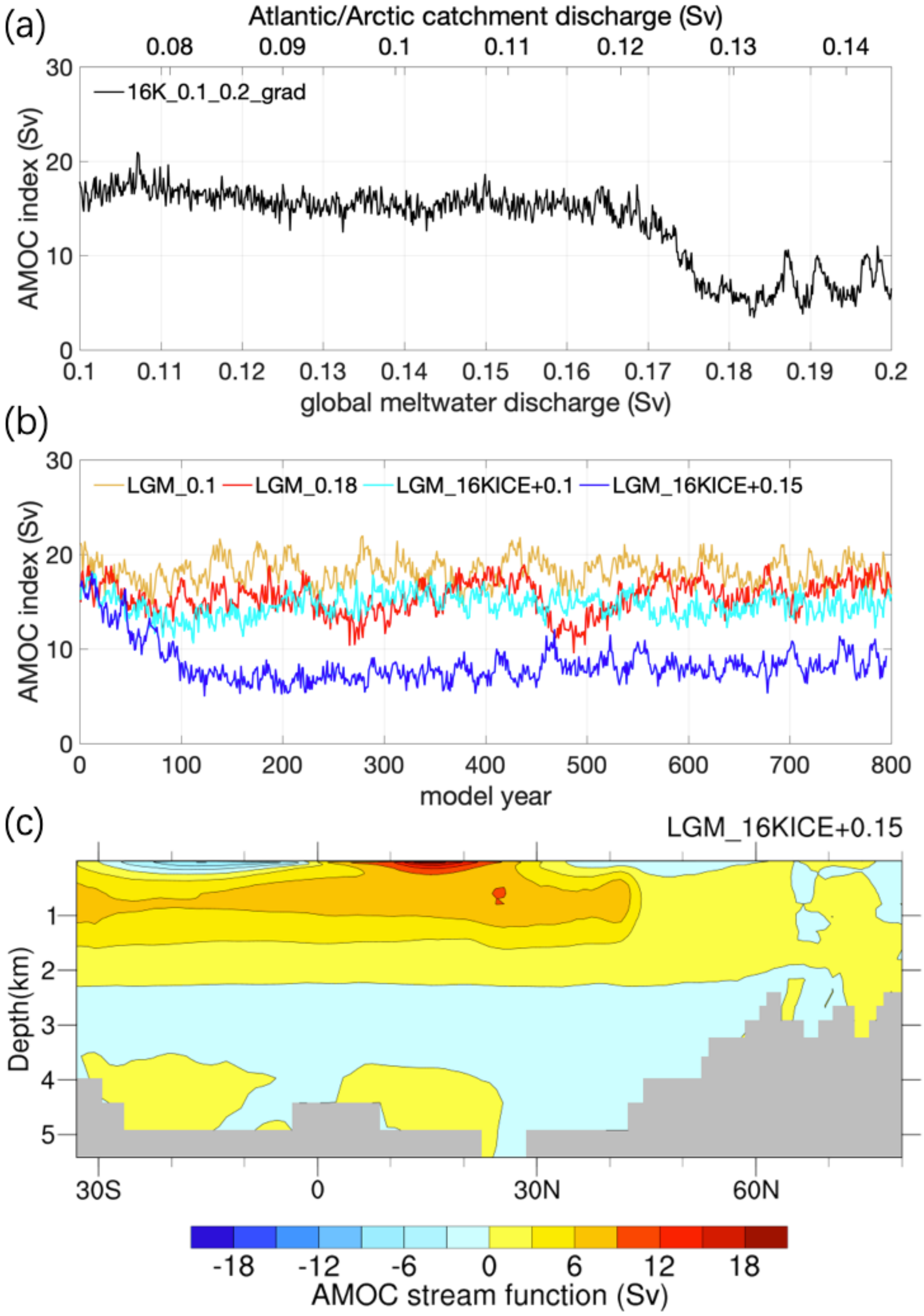

Fig. 3.11 The time evolution of AMOC index (Sv) in experiment 16K_0.1_0.2_grad with a gradual increase of deglacial meltwater discharge from 0.1 to 0.2 Sv based on pattern of MWF2 is shown in panel **a)**. Panel **b)** shows AMOC changes in the experiments with constant discharge for LGM conditions (LGM_0.1 and LGM_0.18) and LGM

conditions, but with reduced ice levels representative of 16 ka (LGM_16KICE+0.1 and LGM_16KICE+0.1). The AMOC stream function (cf. Fig. 3.6) averaged for the last 100 years in LGM_16KICE+0.15 is shown in panel c).

3.3 Discussion and conclusions

The sequence and dynamics of abrupt deglacial events including the LGM-HS1-B/A has been a source of debate. With respect to the HS1-B/A transition our results are consistent with a growing number of studies that identify a gradual deglacial warming as a cause of an abrupt AMOC increase (e.g., Knorr and Lohmann, 2007; Ganopolski and Roche, 2009; Zhang et al., 2017; Obase and Abe-Ouchi et al. 2019), without the necessity to invoke a cessation of North Atlantic meltwater fluxes as a trigger for the B/A (e.g., He et al., 2013; Liu et al., 2009; Menviel et al., 2011). Our results also suggest that the MWF magnitude to attain and sustain a weak HS type AMOC is modulated by the deglacial ice decline and CO_2 increase (Zhu et al. 2014; Galbraith and Lavergene, 2019; Klockmann et al; 2016). More specifically, deglacial ice decline leads to an increased AMOC sensitivity to MWF. Vice versa, a CO_2 rise decreases this sensitivity. Hence, the increased AMOC sensitivity to meltwater for smaller ice sheets might be an alternative key player contributing to a weak HS1-type AMOC without the necessity to have a corresponding meltwater increase. Vice versa, increasing atmospheric CO_2 can lead to abrupt AMOC recovery at the end of HS1 without invoking a corresponding meltwater decrease. Such a framework is complementary to structural changes in the AMOC by CO_2 and ice height changes (Zhang et al., 2014; 2017) that sensitively depend on the interplay of changes in both control factors (Barker and Knorr, 2021). Nevertheless, we highlight here that that neither a freshwater contribution (e.g., 19 ka MWP) to a weak AMOC during HS1 nor a temporal reduction in freshwater just prior to an

AMOC amplification at the onset of the B/A can be ruled out as contributing to AMOC changes into and out-off HS1. For further discussion on the interaction of meltwater and stability changes on AMOC variability during deglaciations we refer to Barker and Knorr (2021).

In summary we conducted a set of sensitivity experiments using boundary conditions of LGM and 16 ka based on state-of-the-art ice sheet and freshwater reconstructions from GLAC-1D (Tarasov et al. 2012). In the experiments without freshwater perturbation, a relatively strong AMOC state is simulated for 16 ka background conditions. The AMOC strength for 16 ka without meltwater perturbation is only slightly weaker than for the LGM and a meltwater perturbation is required to induce and maintain a weaker HS-type AMOC. The MWF threshold for AMOC transition is dependent on the background climate conditions in our experiments. Notably, rising CO_2 increases the threshold, while deglacial ice decline increases the sensitivity of the AMOC to deglacial meltwater.

For 16 ka conditions, a weaker HS-type circulation can be simulated for meltwater fluxes within the range of reconstructions for HS1. Persistent meltwater input below a critical magnitude only causes a temporal weakening of the AMOC, followed by a fast recovery to a strong AMOC state. A local increase in salinity by increasing northward salinity transport gradually strengthens the AMOC. During the weaker phase, heat is accumulated in intermediate water depth in the North Atlantic Ocean, which ultimately leads to an unstable vertical density profile and an abrupt recovery of AMOC. Such a thermal mechanism has been identified by various types of models and data (e.g., Rühlemann et al., 2004; Knorr and Lohmann, 2007; Kim et al., 2012; Li and Born, 2019; Lohmann et al., 2020). It appears that the subsurface warming in conjunction with an increase in surface salinity leads to an unstable weak AMOC state with a subsequent B/A-type warming during the last deglaciation. We find that the destabilizing feedback depends on the AMOC background strength.

Barker and Gregor (2021) propose that increasing atmospheric CO_2 could affects AMOC stability during HS1, outpacing the impacts of declining ice sheet height and eventually triggering a recovery of AMOC as the AMOC is forced to monostable strong (B/A) mode. In this study, we considered the effects of CO_2 rise and ice sheet decline on AMOC separately, but did not consider both factors simultaneously, and therefore could not test this hypothesis. On the other hand, the reconstructed record shows that the significant increase in atmospheric CO_2 concentration (Köhler et al., 2017) appears to be later than the rise in Northern Hemisphere temperatures shown in the ice core record (Kindler et al., 2014) during the onset of B/A. Therefore, we may also need to look for alternative mechanisms (e.g., the change of orbital forcing) that may have led to the recovery of AMOC. We will continue our investigation of these issues in Chapter 4.

In summary, the results in this Chapter highlight the importance of well-constrained (within the constraints of limited paleo data) ice sheet/sea level reconstructions during earlier glacial terminations to compare previous deglaciations to Termination 1 and to better understand the exceptional early timing of the AMOC recovery at the B/A during the last deglaciation.

Chapter 4 Bølling-Allerød revisited

The transition from the Last Glacial Maximum (LGM) to the present interglacial occurred approximately from 21ka to 9ka, known as the last deglaciation and the last ice age termination (Clark et al., 2012; Denton et al., 2010). One remarkable point is that abrupt and significant climate changes occurred during the middle stage of the last deglaciation, superimposing on gradual global warming (Clark et al., 2012; Shakun & Carlson, 2010). Previous studies employed freshwater scenarios to investigate mechanism of abrupt B/A warming event in Termination 1 (Liu et al., 2009; Menviel et al., 2011). In these cases, the response of the climate system to external forcing is linear, where the onset of B/A is triggered by the cessation of meltwater input to the North Atlantic. Recently, increasingly numbers of studies have since begun to focus on dependence of AMOC stability on climate to explain the associated abrupt climate changes, such as gradual changes in ice volume (Zhang et al. 2014) and gradual changes in atmospheric CO_2 concentration (Zhang et al. 2017). In this context, the occurrence of B/A was recently simulated by Obase and Abe-Ouchi (2019) in the presence of freshwater forcing through rising atmospheric CO_2. However, as the authors suggested, the freshwater forcing in their experiments resulted in weaker equivalent sea level (ESL) change than the reconstructed record and did not consider changes in ice volume during this period, indicating the lack of convincing transient experiments related to the more realistic boundary conditions.

In this chapter, we investigate changes in the AMOC with respect to multiple forcings and transient boundary conditions during deglaciation, including changes in atmospheric CO_2 concentration, continental ice sheets, and orbital forcing by a suite of simulations with the water isotope enabled fully-coupled ocean-atmosphere-sea ice-land surface model COSMOS-wiso. Consistent with chapter 3, Ice Sheet changes, including associated deglacial meltwater and iceberg fluxes, are still based on the state-of-the-art GLAC-1D reconstruction (Tarasov et al., 2012). The simulations are used to explore physical mechanisms for the occurrence of AMOC abrupt change. Meanwhile, the simulated water isotopes can validate our results by providing a one-to-one comparison with proxy records at B/A warming.

4.1 Experimental design

In the following section we describe the experimental set-up of the model simulations in this chapter. An overview of experimental details is provided in Table 4.1.

Table 4.1 An overview of experimental details for all the simulations in this study

ID	Initial Ocean State	Fixed Boundary/Forcing	Transient Boundary/Forcing
Spin-up simulation			
16k-spinup	LGM	Ice-sheet height, Ice-sheet extent, GHG, Insolation & MWF	/
Transient simulations			
TRN-full	16 ka	/	Ice-sheet height, Ice-sheet extent, GHG, Insolation & MWF
TRN-FW	16 ka	MWF	Ice-sheet height, Ice-sheet extent, GHG & Insolation
TRN-FW-GHG	16 ka	Ice-sheet height, Ice-sheet extent, Insolation & MWF	GHG
TRN-FW-ICEa	16 ka	GHG, Insolation, MWF & Ice-sheet height	Ice-sheet extent
TRN-FW-ICE	16 ka	GHG, Insolation & MWF	Ice-sheet height & Ice-sheet extent
TRN-FW-ICEGHG	16 ka	Insolation & MWF	Ice-sheet height, Ice-sheet extent & GHG
TRN-FW-ORB	16 ka	GHG, Ice-sheet height, Ice-sheet extent & MWF	Insolation
TRN-TraCE	16 ka	/	Ice-sheet height, Ice-sheet extent, GHG, Insolation & MWF
Equilibrium simulations			
16K-FW	16 ka	All BCs are consistent to TRN-FW at 16 ka	
E-FW-15k	TRN-FW at 15 ka	All BCs are consistent to TRN-FW at 15 ka	
E-FW-14.8k	TRN-FW at 14.8 ka	All BCs are consistent to TRN-FW at 14.8 ka	
E-FW-14.6k	TRN-FW at 14.6 ka	All BCs are consistent to TRN-FW at 14.6 ka	

4.1.1 Full forcing transient experiments

We conducted transient simulation (TRN-full) from a glacial state at 16 ka towards B/A following the protocol of PMIP4 (Ivanovic et al., 2016). Ice sheets and surface topographies are prescribed from GLAC-1D reconstructions. In the global MWF, freshwater due to melting ice-sheets is distributed in the offshore region, while freshwater due to ice calving in Northern Hemisphere is uniformly released in the IRD belt (cf. section 2.2). The coastlines and bathymetry are fixed to those of the LGM throughout the simulations to remove the complex influence of water tunnel change on the AMOC. The ice sheets configuration in the transient experiments are shown in Fig.4.1 and Fig. 4.2. Besides this full forcing transient experiment, we also produced a similar run but with constant MWF (TRN-FW). This MWF of 0.15 Sv is taken from the average between 16 ka and the end of HS1-B/A transition (14.5 ka) in GLAC-1D, which is global 0.15 Sv (1 Sv = 10^6 m^3s^{-1}). The ESL change resulted from this freshwater forcing is in the range of estimated uncertainty from proxy data (Deschamps et al., 2012; Fig. 4.3). To evaluate consequences of different freshwater scenarios on AMOC variation, we also conduct a full transient experiment (TRN-TraCE) with MWF scheme from the TraCE-21ka simulation (Liu et al., 2009; Fig. 4.3).

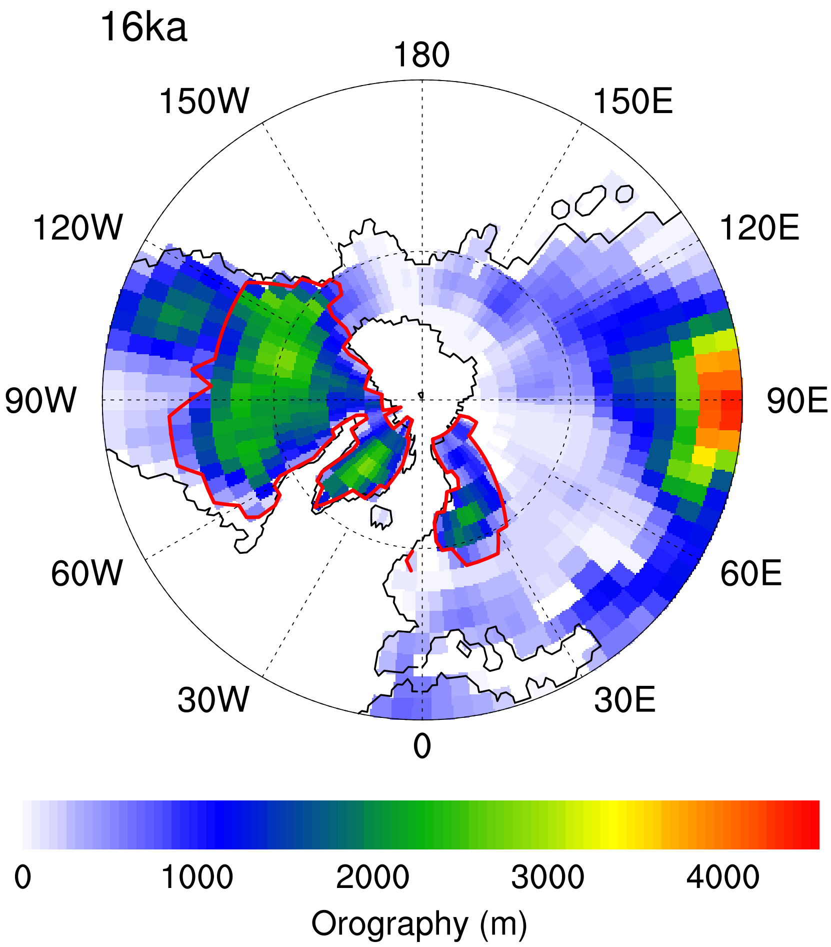
16ka
180
150W
150E
120W
120E
90W
90E
60W
60E
30W
30E
0
0
1000
2000
3000
4000
Orography (m)

Fig. 4.1 Orography (m) at 16 ka from GLAC-1D in the Northern Hemisphere. The ice sheet extent is indicated by red lines. The black lines in represent the coastline at the LGM.

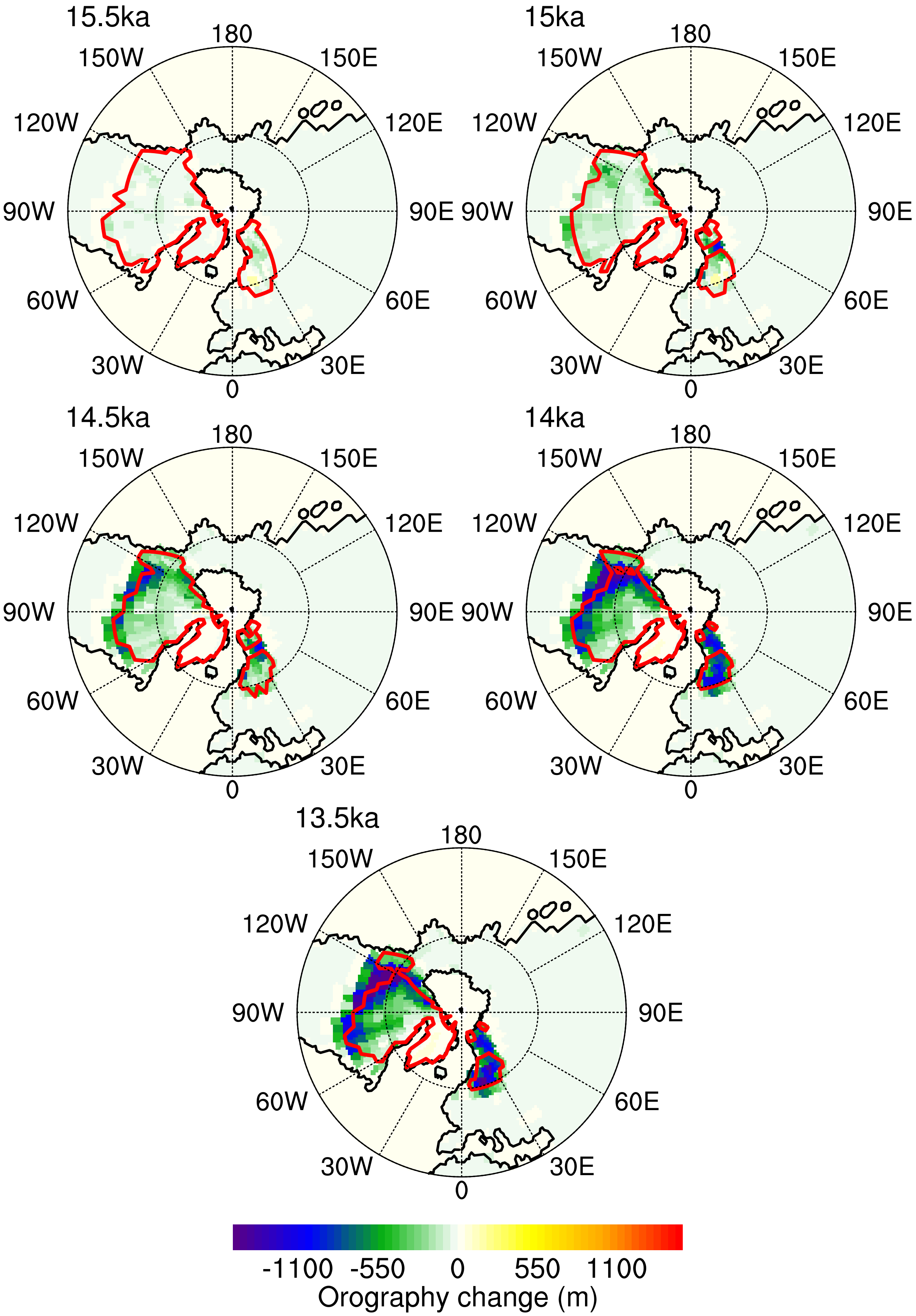
15.5ka
15ka
14.5ka
14ka
13.5ka
180
150W
150E
120W
120E
90W
90E
60W
60E
30W
30E
0
-1100 -550 0 550 1100
Orography change (m)

Fig. 4.2 Northern Hemisphere orography differences from 16 ka in different time. The black and red lines are same as in Fig. 4.1.

4.1.2 Single forcing transient experiments

To disentangle and quantify the effects of different factors on the climate system during this period, we conducted a series of sensitive experiments with changes of in GHG, orbital forcing and ice-sheet configuration under the background with persistent freshwater forcing. The freshwater forcing in these sensitivity experiments were all averaged over the period 16 ka to 14.5 ka in GLAC-1D, implying that effects introduced by the temporal variability of freshwater scenario were excluded. Each sensitivity experiment thus can assess roles of change in a single transient forcing. Regarding ice sheet change, we conducted two experiments to separate roles of changes in ice-sheet height and extent. In TRN-Lev015-ICE, both height and extent are considered. While in TRN-Lev015-ICEa, change in ice-sheet extent/area is considered, while its height is fixed at the 16-ka level. To assess potential synergic effects, an experiment imposed by both ice sheet and atmospheric CO_2 concentration change is conducted. Besides the transient forcing runs, an equilibrium run under 16 ka boundary condition with persistent freshwater forcing (0.15Sv) is conducted as the control experiment. By analyzing simulated AMOC variation in different experiments and the timing of AMOC mode changes, we can evaluate contributions of different forcing factors to abrupt B/A warming as well as the relevant physical mechanisms. To pin down the governing dynamics inferred, we also carried out snapshot sensitivity experiments with fixed boundary conditions (E-FW-15k, E-FW-14.8k, and E-FW-14.6k), which are initializing from different time points in TRN-full.

4.1.3 Water isotope configuration

The water cycle is a key component of the Earth's climate system. Water stable isotopes ($H_2^{18}O$, $HD^{16}O$, and $H_2^{17}O$) are integrated tracers of climate processes occurring in various branches of this cycle (Craig and Gordon, 1965; Dansgaard, 1964). To the first order, water stable isotopes (hereafter expressed in a δ notation as $\delta^{18}O$ and δD with respect to the Vienna Standard Mean Ocean Water standard V-SMOW, if not stated otherwise) in polar ice cores are used for past temperature reconstructions over the past glacial–interglacial cycles (Jouzel et al., 2007; NEEM community members, 2013). However, while records of water isotopes in natural archives provide key documentation of past climate variations, their quantitative translation to climate variables such as temperature or precipitation amount still remains uncertain in many cases. To provide a direct comparison of water oxygen isotopes between proxy records related to the HS1-B/A period and our model outputs, we used the water-isotope-enabled version of COSMOS developed by Werner et al. (2016) to conduct the transient simulations mentioned in this chapter.

The water isotope distribution has been taken from an already equilibrated LGM simulation (Werner et al., 2016). This LGM experiment has been integrated for 4500 years and the simulated isotope is broadly consistent with observations. After the spin-up experiment, the information of water isotopes was applied to the transient experiments starting from 16ka (Fig.4.3).

(a) δ^{18}O in precipitation

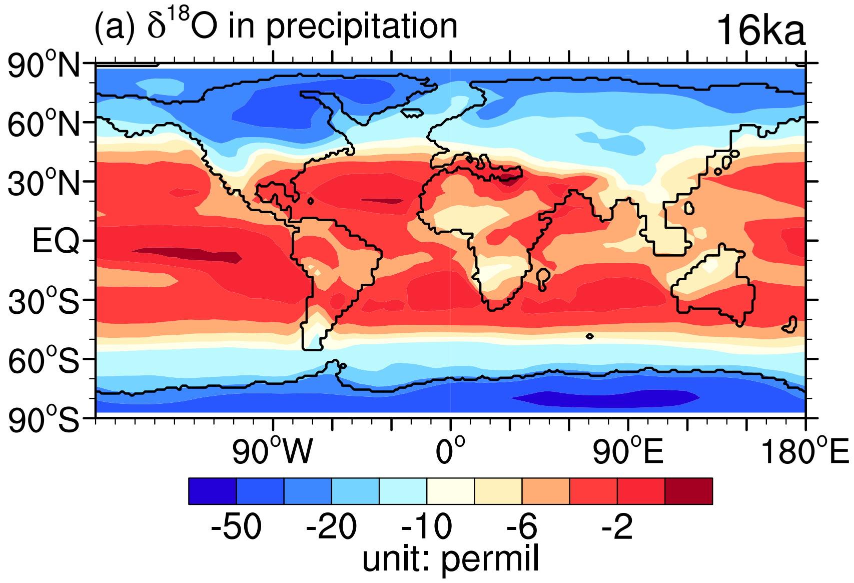
16ka
90°N
60°N
30°N
EQ
30°S
60°S
90°S
90°W
0°
90°E
180°E
-50
-20
-10
-6
-2
unit: permil

(b) δ^{18}O in surface water

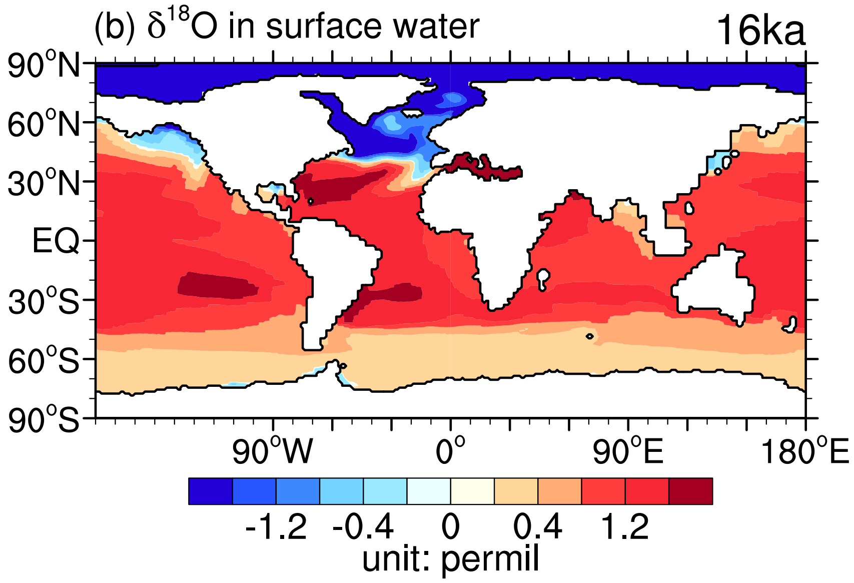
16ka
90°N
60°N
30°N
EQ
30°S
60°S
90°S
90°W
0°
90°E
180°E
-1.2
-0.4
0
0.4
1.2
unit: permil

Fig. 4.3 Global distribution of simulated annual mean δ^{18}O values in precipitation (a) and ocean surface waters (b) at 16 ka.

4.2 Results

4.2.1 Role of different freshwater histories in B/A warming

Fig.4.4 shows the AMOC response to different freshwater scenarios. TRN-full is responsible for a full transient forcing with a purpose of mimicking real MWF, while TRN-FW and TRN-TraCE are in general as sensitivity runs. The magnitude of global MWF reconstructed by

GLAC-1D is weaker than 0.1 Sv for most of the late H1 period (Fig. 4.4c-d). In such a freshwater background, neither the equilibrium experiments shown in Chapter 3 nor the transient experiment demonstrated here indicated a weak AMOC mode during the HS1 as indicated by reconstructed records (e.g., Ng et al., 2018). Specifically, the amount of freshwater gradually increased until 15.4 ka, but still not enough to weaken the AMOC. Then, the total amount of freshwater reached 0.1 Sv at 15.4 ka, and the AMOC began to weaken and reached a minimum at 15.1 ka. After that, along with weakening discharge, the AMOC quickly returned to the strong mode. Finally, the Meltwater Pulse 1a (MWP1a), which starts at 14.7 ka, makes the AMOC enter into the weak mode again. The intensity of AMOC was significantly modulated by the amount of freshwater during this process. In another study, by applying MWF calculated from either GLAC-1D or ICE-6G to the transient simulations in the last deglaciation, both two experiments showed a similar response to the MWF (Kapsch et al., 2022). The weak freshwater forcing during HS1 and the strong freshwater forcing during B/A prevent the model from accurately reproducing the HS1-B/A transition.

Liu et al. (2009) obtained the weak AMOC mode by persistently injecting large amounts of freshwater flux in the North Atlantic during the late H1. An abrupt increase in the AMOC was simulated in response to cessation of meltwater input at the onset of B/A. We used the same freshwater forcing in the COSMOS model to repeat this experiment and obtained similar results (TRN-TraCE in Fig. 4.4g). Sea-level reconstructions indicate a massive input of meltwater during the early stage of the last deglaciation (Fairbanks et al., 1992). Most of the meltwater likely originated from the decaying Laurentide ice sheet during the Bølling period. A sudden stop of freshwater is therefore an unlikely explanation of the deglacial sequence during the Bølling interstadial.

TRN-TraCE also demonstrates the linear response of the system to the forcing. According to this mechanism, a large amount of freshwater injection in the key convection sites of NA is required to suppress the formation of the NADW. In contrast, according to the freshwater strategy of GLAC-1D, a significant portion of freshwater will enter the ocean along the shorelines and thus will not enter the mixing zone directly. Therefore, to gain a more realistic results during HS1 in TRN-full, a stronger discharge amount is required. This reflects the critical influence of freshwater distribution on AMOC in the COSMOS model. On the other hand, the excessive amount of freshwater during the B/A period made the time of AMOC recovery differ significantly from the proxy record. We have therefore modified the freshwater scenario calculated from GLAC-1D. This MWF is taken from the average between 16 ka and the end of the HS1-B/A transition (14.5 ka), which is 0.15 Sv and remains in the uncertainty of ESL change. From Chapter 3, we have already known that the sensitivity of AMOC to freshwater forcing changes as the boundary conditions change during the last deglaciation. Hence, a fixed freshwater forcing may also trigger AMOC to undergo a mode transition. Based on this strategy, TRN-FW shows a stadial climate during H1 and also captures the HS1-B/A AMOC recovery (Fig. 4.4c). Although the time of the B/A event in the experiment is not consistent with the TRN-TraCE, the time of AMOC recovery here is closely related to the freshwater forcing, and there is some randomness in whether the AMOC can recover at the proper time. If the cost of the model simulation is not considered, running a large number of sensitivity experiments with a slight change in the MWF field will likely yield results that are more consistent with the proxy data. Therefore, in this study, we only consider the mechanism of AMOC change and do not focus on the timing of B/A occurrence.

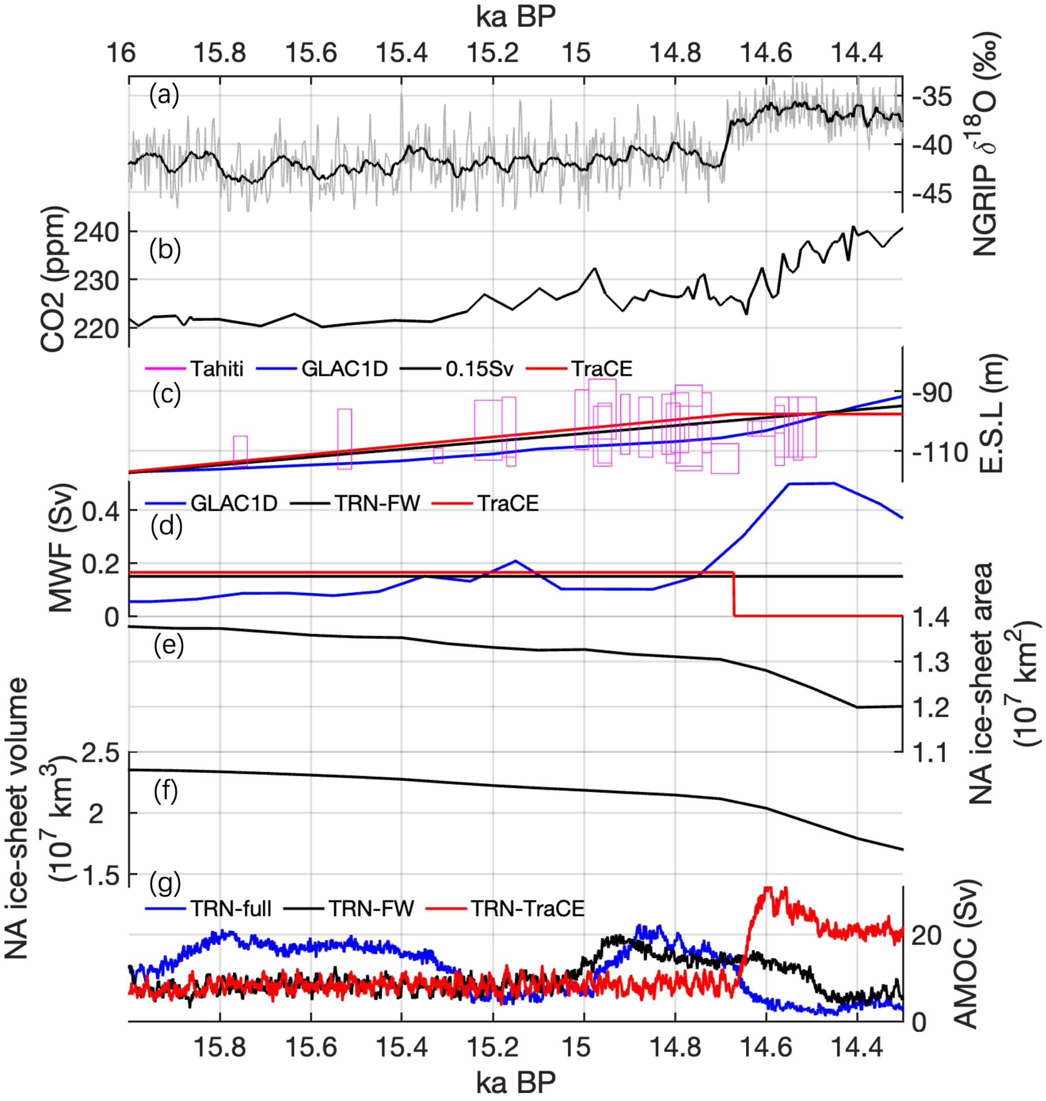

Fig. 4.4 **a)** NGRIP Greenland ice-core δ^{18}O. **b)** CO$_2$ volume from Köhler et al., 2017. **c)** Equivalent sea level change calculated from GLAC-1D (black) and far-field relative sea level records from Tahiti (Deschamps et al., 2012) **d)** Temporal evolution of the total global MWF (Sv) used in TRN-full (blue), TRN-FW (black) and repeated TraCE-21ka experiment (red). **e)** Ice-sheet area change in the North America (NA) **f)** Ice-sheet volume change in the NA **g)** Time evolution of the AMOC (Sv) for transient FW (blue), constant FW (black) and repeated TraCE-21ka experiment (red). Bold line in a) represents 50 yr running-mean values.

4.2.2 Model-data Comparison

In experiments considering the original GLAC-1D freshwater forcing, AMOC experienced twice weak to strong mode transitions at ~15.9 ka and ~15 ka, respectively, prior to the MWP1a freshwater event (TRN-full in Fig. 4.4g). Between them, the second recovery is more consistent with the time of B/A occurrence. Thus, the HS1-B/A transition is present in all three transient experiments considering different freshwater scenarios. Given the availability of water isotopes in our model, we can directly compare the results of these three experiments with the proxy data. Thus, we can examine the approximation of the simulation results to the indicators under different B/A occurrence mechanisms.

By comparing with the δ^{18}O from North Greenland Ice Core Project (NGRIP, Kindler et al., 2014), we found a possible systematic bias of about 8 permille in the simulated δ^{18}O isotopes in the precipitation (Fig, 4,5a). After further aligning the simulated results with the proxy data at the respective B/A occurrence time points, we found that the intensity of the B/A events simulated by TRN-TraCE is closest to the proxy data. In the experiments using GLAC-1D freshwater forcing, the amplitude of HS1-B/A transition events was about one-half that of TRN-TraCE and one-fourth that of the ice core data (Fig. 4.5b). The smaller amplitude is mainly due to the fact that the recovery of AMOC during B/A events is constrained by the background freshwater and cannot achieve the dramatic AMOC overshoot like in the TRN-TraCE experiments. While in the comparison with the NGRIP temperature reconstruction data, the experiments using GLAC-1D freshwater forcing both exhibit significant HS1-B/A transition with an intensity of about one-half of the reconstruction record (Fig. 4.5c-d). This demonstrates that the AMOC recovery mechanism in the presence of background freshwater can also partially explain the phenomena recorded in the proxy data.

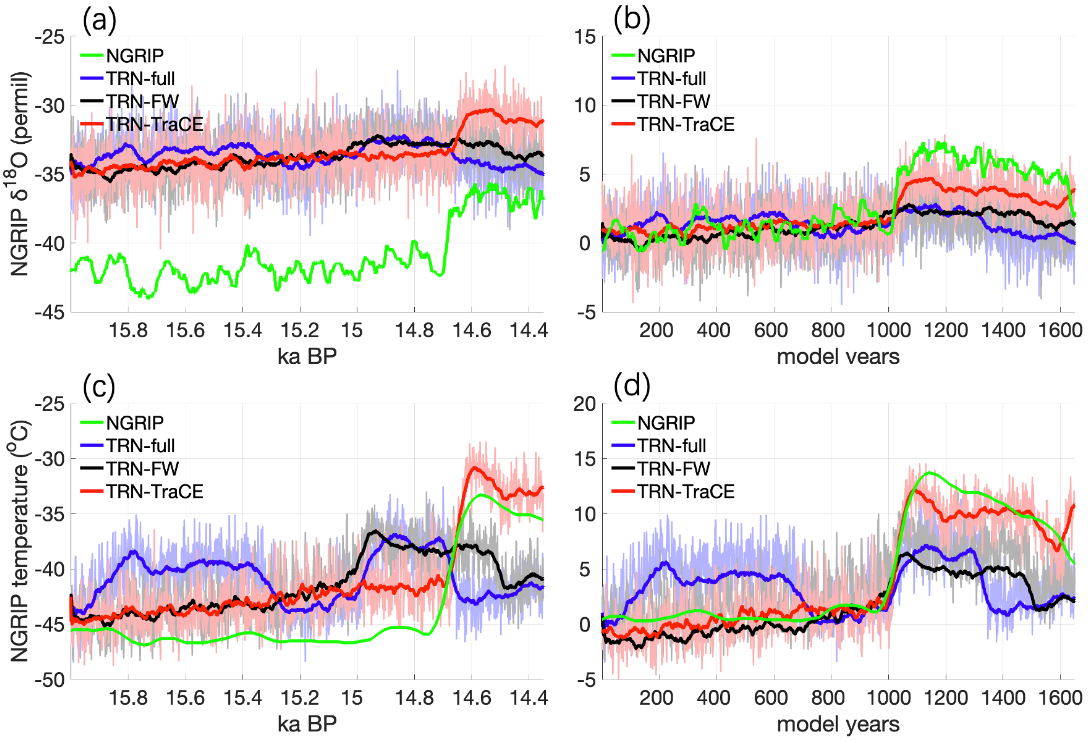

Fig. 4.5 a, c) Simulated NGRIP δ^{18}O in precipitation and surface temperature together with the NGRID ice core data. b, d) The NGRIP results of each experimental simulation were aligned to the time when the B/A transition occurred, respectively. Bold lines represent 50 yr running-mean values.

4.2.3 B/A warming—an expression of AMOC self-oscillation

In addition to freshwater forcing, decreases in Northern Hemisphere ice volume and increases in atmospheric CO_2 concentration during HS1-B/A transition period may also affect the timing of AMOC recovery (e.g., Zhang 2014, 2017; Barker & Knorr 2021). In Chapter 3, we considered the effects of CO_2 rise and ice sheet decline on AMOC separately, but did not consider both factors simultaneously. Besides, the ice-sheet is becoming smaller in extent as it melts, and the resulting changes in surface albedo may heat the Northern Hemisphere. It is also uncertain whether this process will affect the timing of B/A transition. Therefore, a set of sensitivity transient experiments regarding these boundary conditions change is necessary.

Since the fixed MWF forcing experiment TRN-FW shows a more reasonable result and is unaffected by the temporal variability of discharge, the following sensitive experiments is produced with the same MWF field. The key experiments are shown in Fig.4.6 and the others are shown in Fig. 4.7.

In both TRN-FW-ICEGHG and TRN-FW-ICE ice-sheet height decline is imposed. Except for these two experiments, AMOC in the other runs recover at different time. The recovery mechanism is similar to the demonstration in section 3.2.1. As heat accumulated in the subsurface ocean, sea-air interactions create positive feedback processes that destabilized the vertical stratification. This, in addition to simultaneous enhancement of northward salinity transport, eventually leads to the recovery of AMOC. The time series analysis of the four key experiments in Fig.4.6 regarding the recovery mechanism of AMOC is presented in Fig. 4.8.

We noticed that except TRN-FW-GHG, in all the experiments where AMOC recovered, AMOC returned to the weak mode after recovery. And in the single orbital forcing and glacial area runs, AMOC will enter into the strong mode for the second time. This implies that the AMOC in these experiments might be in a self-oscillatory regime. Here, we take TRN-FW as an example to demonstrate the process after AMOC recover. When AMOC is in weak mode, the sea ice in the northeastern North Atlantic (NENA, the main convection site) continuously melts. When reaching the critical point, sea ice melts rapidly, allowing the subsurface heat to be released and causing the recovery of the AMOC. When the heat release is completed, the sea ice grows again, stabilizing the stratification and weakening the AMOC. As a result, heat accumulates in the subsurface layer for the second time (Fig. 4.9).

A recent study pointed out that the variation of solar radiation at high latitudes in the Northern Hemisphere caused by the change of obliquity and the variation of solar radiation at low latitudes caused by the change of the eccentricity induced precession have critical impact on the occurrence of self-oscillation (Zhang et al., 2021). According to the results from our transient runs, we therefore hypothesize that the AMOC recovery process in the full forcing experiment is associated with this self-oscillation mechanism.

First, we branched equilibrium state experiments from TRN-FW to demonstrate whether the system was in self-oscillation during the period from late H1 to B/A, or was in self-oscillation for a certain period (i.e., passed through the self-oscillation window). These experiments are initialized from several different moments in the TRN-FW (Fig. 4.6e-g). E-FW-15k starts from the moment when the AMOC starts to recover in TRN-FW. In this experiment, the AMOC first completes the transition from the weak to the strong mode and returns to the weak mode a few hundred years later, similar to the control run. Both E-FW-14.8k and E-FW-14.6k start from the moment after the recovery of the AMOC in TRN-FW. The AMOC in both experiments undergoes a strong to weak mode transition and appears in a second oscillation cycle that is not present in the control run. These three equilibrium experiments demonstrate the existence of a self-oscillation window during the period from 15ka to 14.6ka.

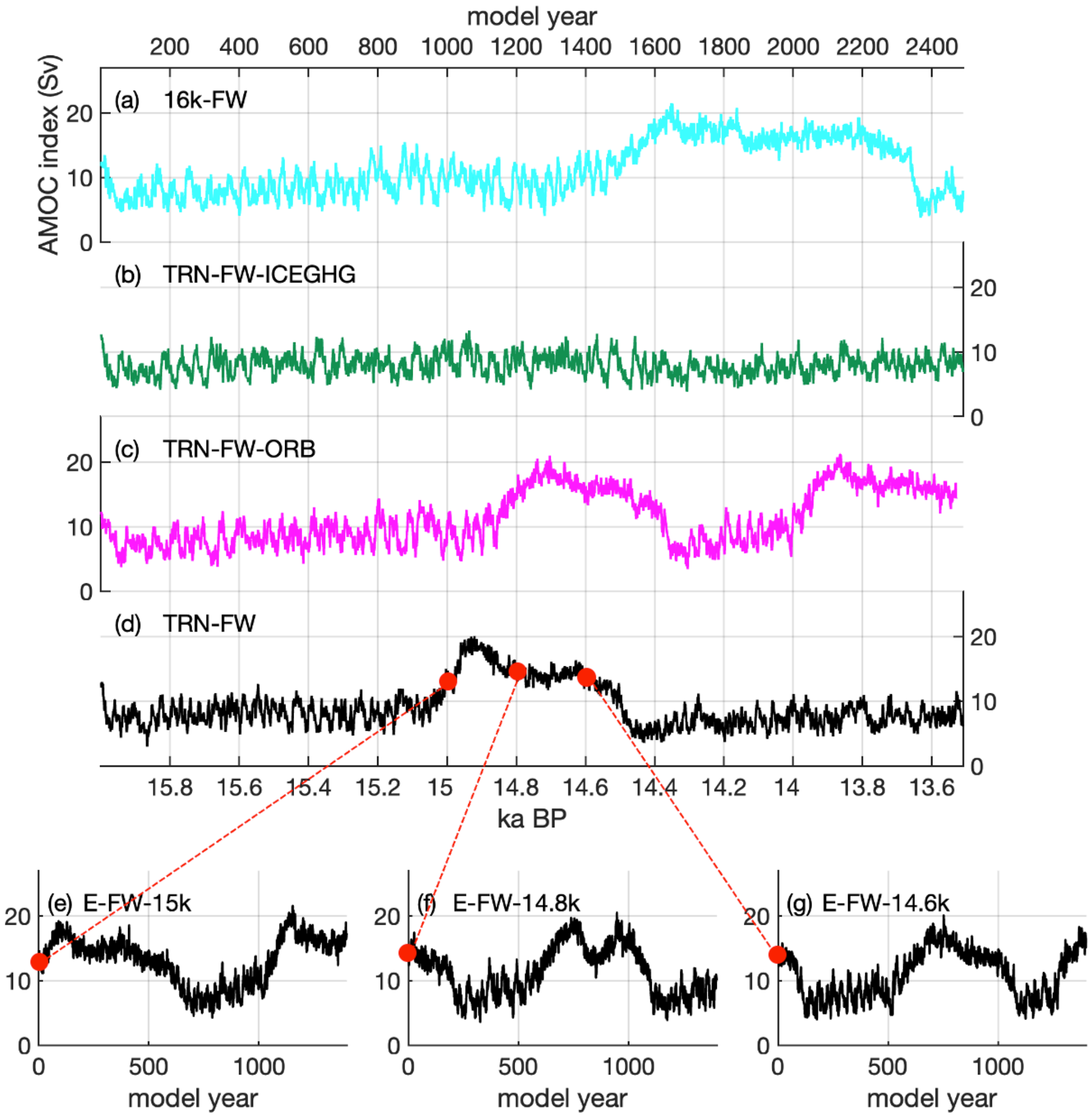

Fig. 4.6 Time evolution of the AMOC (Sv) for the sensitivity experiments. All the experiments shown here contain the same freshwater forcing applied in TRN-FW a) Equilibrium run under 16 ka boundaries. b) Transient experiments considering both GHG and ice-sheet change. c) Transient experiments considering only insolation change. d) Transient experiments considering all forcing. e-g) equilibrium runs branched from 15ka, 14.8ka and 14.6ka in TRN-FW, respectively.

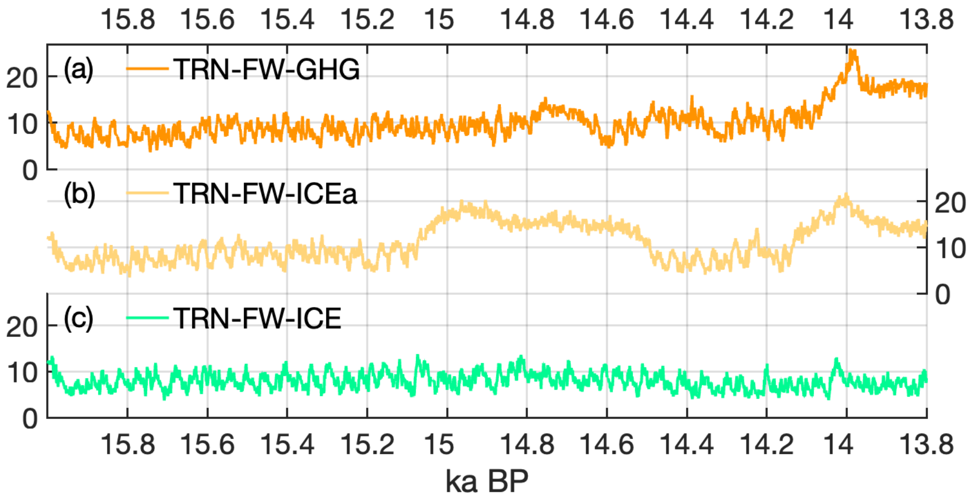

Fig. 4.7 Similar to Fig. 4.6. **a)** Transient experiments considering only GHG change. **b)** Transient experiments considering only ice-sheet extent change. **c)** Transient experiments considering complete ice-sheet change.

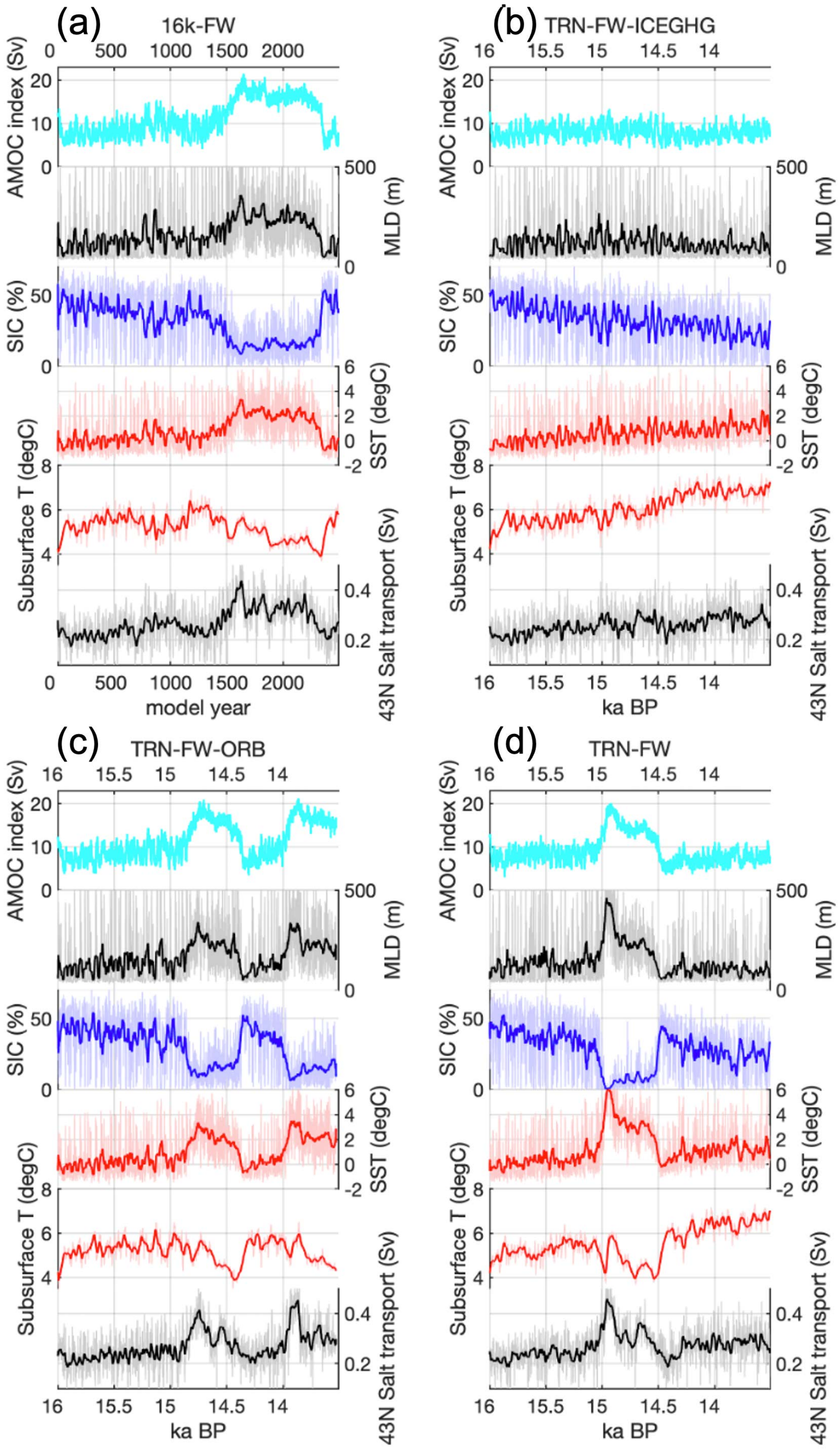

Fig. 4.8 (a-d) AMOC abrupt change dynamics in the experiments shown in Fig.4.6 (a-d), respectively. SST, SIC and subsurface T are calculated as the regional averages of the NENA (30°W-20°W, 56°-64°N).

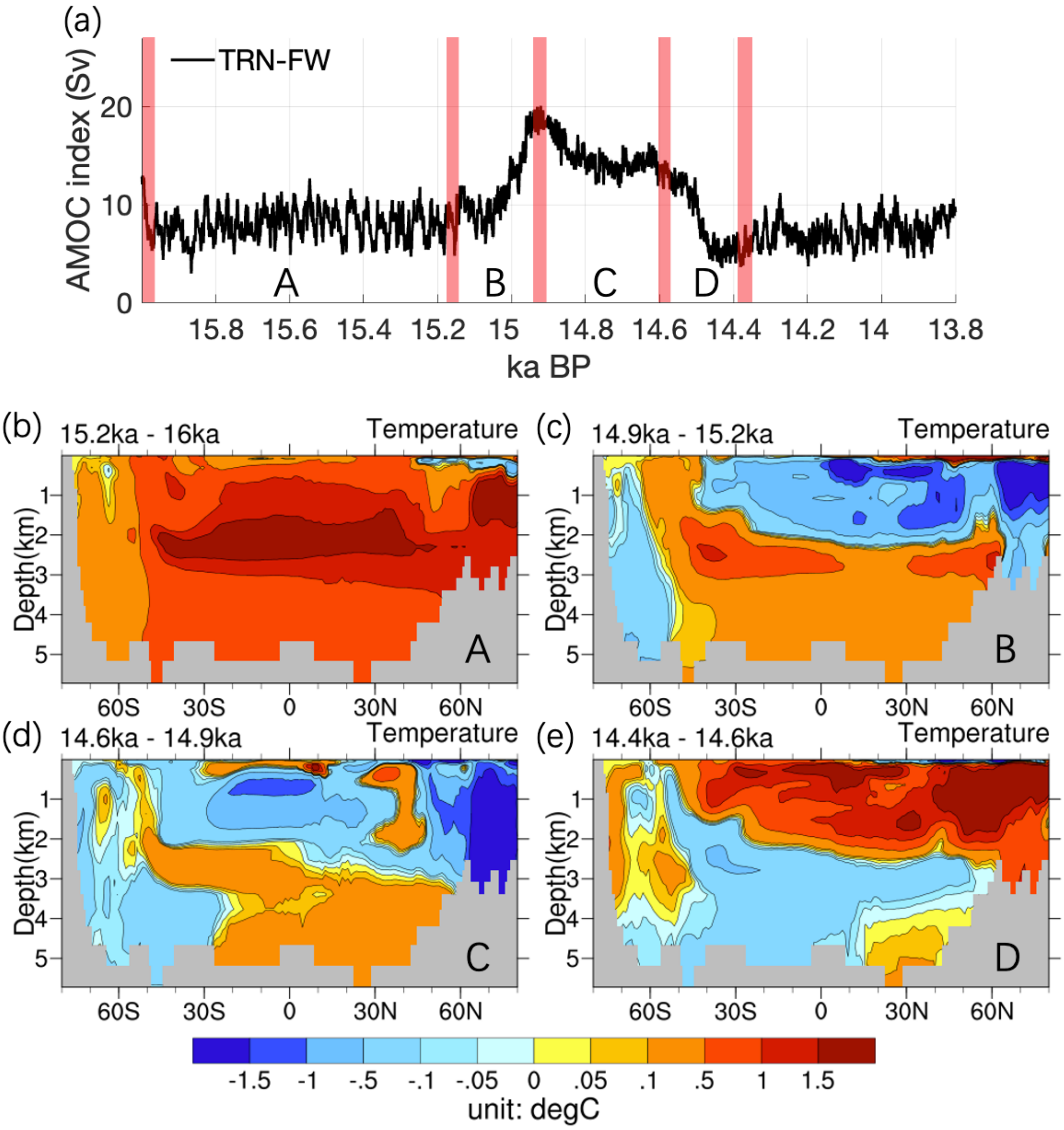

Fig. 4.9 a) Time evolution of the AMOC (Sv) for TRN-FW. Letters A-D define different time period in the simulation. **(b-e)** Temperature anomaly during different phase of TRN-FW (letters shown in panel **a)**) in the Atlantic section. **b)** 15.2ka minus 16ka; **c)** 14.9ka minus 15.2ka; **d)** 14.6ka minus 14.9ka; **e)** 14.4ka minus 14.6ka

4.2.4 Govern dynamic of AMOC self-oscillation

Previous studies have shown that the HS1-B/A transition occurs due to the combined control of CO_2 and ice volume. However, in our sensitivity experiments considering only CO_2 and ice volume change, no AMOC recovery occurred before 13 ka (Fig. 4.6b). Different from the other runs, the mixing in TRN-FW-ICEGHG in the main convection area is keeping in a low level during the entire time (Fig. 4.8b), and it shows a decreasing trend starting from 15 ka.

Our model simulations show that in the stadial climate, Laurentide Ice Sheet (LIS) splits the northern and southern branch of the westerly winds in different directions (Contours in Fig. 4.11). Previous studies have shown that reducing the height of the LGM LIS causes the northern branch of the westerlies to shift southward while the southern branch weakens. Zhang et al. (2014) simulated a westerly core located at ~53°N when reducing the ice volume to a level of 14.5 ka, which facilitates the transport of sea ice generated in the Labrador Sea to the Irminger Sea. This increases the sea ice concentration and results in a surface cooling over the region, preventing open ocean convection and the reformation of NADW.

In our transient experiments, the ice sheets configuration is set up from the GLAC-1D reconstruction results. As seen in Fig. 4.2 the southern boundary of the LIS gradually moves northward and the decay in height is concentrated on the southern edge of the ice sheet. This leads to a gradual northward shift of the southern branch of the simulated westerlies and a weakening of the northern branch. The zonal wind stress from 40°N to 45°N gradually strengthens and sea ice generated in the Labrador Sea is transported to the North Atlantic from a more southerly location. Sea ice transported southwards melts rapidly and significantly reduces local salinity. The less saline water is transported over the North Atlantic Ocean via the North Atlantic Current (NAC). The reduction of SSS in the mixing zone will weaken the seawater stratification and reduce the generation of NADW. The reconstructed ice sheet results showed that ice sheet melting started to accelerate after 14.5 ka (Fig. 4.4e-f), and this process can be developed (Fig. 4.10, Fig. 4.11).

TRN-FW-ICEGHG suggested that change in CO_2 alone is not sufficient to overcome the potentially strong freshwater forcing and ice-sheet decrease effect and lead to a B/A event during this period. The difference between the TRN-FW-ICEGHG and the full forcing experiment is that the variation of the orbital parameters is not considered in the former. In the transient experiment with single orbital parameter forcing (TRN-FW-ORB), AMOC change is characterized by two self-oscillation cycles. Compared with the control run, the AMOC recovers earlier and with shorter oscillation periods in TRN-FW-ORB. However, AMOC recovers later and does not recover again after completing one self-oscillation cycle in the full-forcing experiment. We infer that change of orbital parameters during this period may be the reason for the existence of self-oscillation, while persistent changes in ice sheet and atmospheric CO_2 drive the AMOC out of its oscillatory regime. This process may be the mechanism behind the HS1-B/A transition.

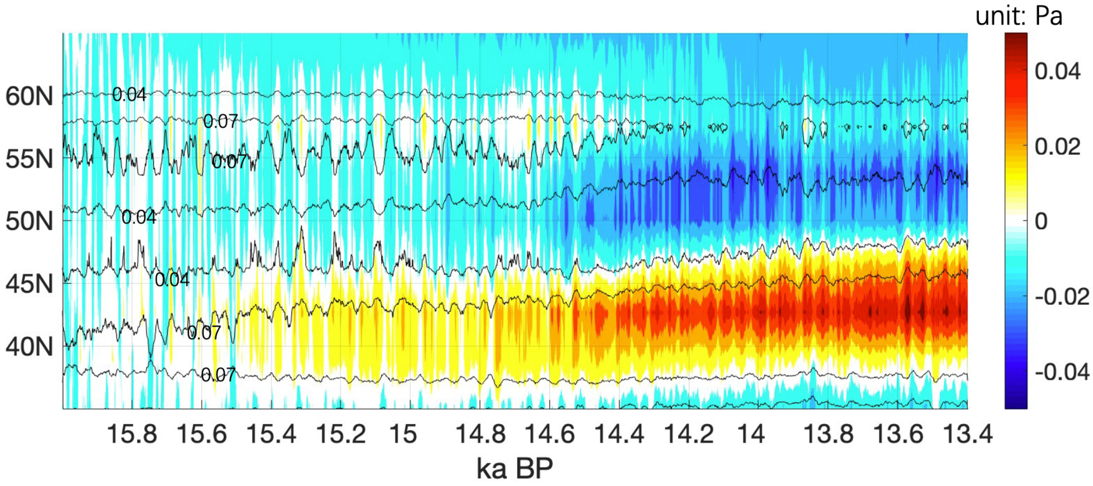

Fig. 4.10 Zonal mean wind stress (Pa) anomaly along 100°W-40°W in TRN-FW-ICEGHG. Contour shows zonal mean wind stress. The data is smoothed by 10 yr running-mean.

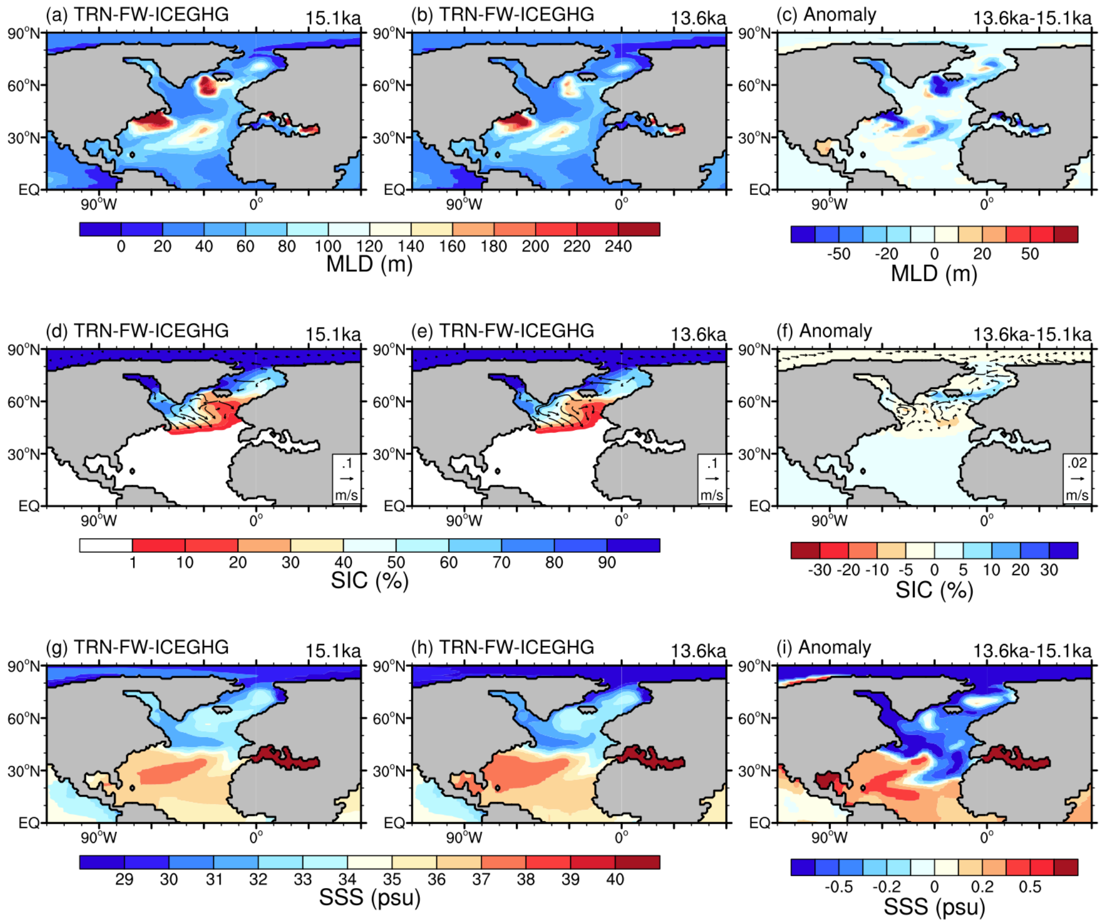
(a) TRN-FW-ICEGHG
15.1ka
(b) TRN-FW-ICEGHG
13.6ka
(c) Anomaly
13.6ka-15.1ka
90°N
60°N
30°N
EQ
90°W
0°
0 20 40 60 80 100 120 140 160 180 200 220 240
MLD (m)
-50 -20 0 20 50
MLD (m)
(d) TRN-FW-ICEGHG
15.1ka
(e) TRN-FW-ICEGHG
13.6ka
(f) Anomaly
13.6ka-15.1ka
.1 m/s
.02 m/s
1 10 20 30 40 50 60 70 80 90
SIC (%)
-30 -20 -10 -5 0 5 10 20 30
SIC (%)
(g) TRN-FW-ICEGHG
15.1ka
(h) TRN-FW-ICEGHG
13.6ka
(i) Anomaly
13.6ka-15.1ka
29 30 31 32 33 34 35 36 37 38 39 40
SSS (psu)
-0.5 -0.2 0 0.2 0.5
SSS (psu)

Fig. 4.11 a-c) Simulated mixed layer depth in TRN-FW-ICEGHG at 15.1ka **(a)**, 13.6ka **(b)**, and the anomaly between these two times (c); **d-f)** same as **a-c)**, but for sea ice compactness; **g-i)** same as **a-c)**, but for sea surface salinity.

4.3 Discussion and conclusions

A fundamental issue is how to obtain an appropriate stadial state for the H1 and to simulate the subsequent a series of abrupt climate change. In the transient framework, the HS1 and B/A sequence cannot be correctly simulated by the forcing concept as suggested by the PMIP4 protocol (Ivanovic et al., 2016). Based on this concept, we find two main features regarding applying reconstructed MWF timeseries in the transient simulation. One is the inability to simulate a weak AMOC during the HS1 period, and the other is the inaccurate timing of the simulated abrupt warming during the Bølling. Our transient simulation shows a weakened AMOC with North Atlantic cooling during the Bølling interstadial. These issues are also revealed in other simulations (Kapsch et al., 2022). The main reason is that the freshwater forcing in the experiments is not appropriate in understanding mechanisms and processes that acted during the last deglaciation.

In the model-data comparison, all three experiments considering different freshwater scenarios simulated the water isotope changes associated with the HS1-B/A transition. The different timing of AMOC abrupt change in the simulations might depend on the amount of the prescribed freshwater flux.

Sea-level reconstructions indicate a massive input of meltwater during the early stage of the last deglaciation. Most of the meltwater likely originated from the decaying Laurentide ice sheet during the Bølling period. A sudden stop of freshwater is therefore an unlikely explanation of the deglacial sequence during the Bølling interstadial. As a different scenario, our model is able to simulate the occurrence of the HS1 and Bølling sequence, even under a constant freshwater forcing, but varying other boundary conditions. This suggests that the AMOC abrupt change in the end of last ice age is not a linear response to external forcing, but rather is determined by the existence of an instability window in the presence of multiple changing boundary conditions

The self-oscillation characterizes the simulated HS1-B/A transition with fixed MWF. This feature will no longer exist in the scenario where the variation of orbital parameters is not considered, thus indicating the critical role of the orbital forcing. Meanwhile, the system has the ability to pass the self-oscillation window as other boundary conditions change, especially for the ice sheet. This potential mechanism may help us to explain why the AMOC recovery in the full forcing experiment did not occur at 14.7 ka when the abrupt climate transition was recorded in the ice-core data. Since the temporal variation of the freshwater forcing was not considered in our experiments, the slight difference in the amount of freshwater and the difference in the distribution into the ocean may lead to a large variation in the timing of the AMOC model change occurs. The B/A event can be resulted from the response to the combination of ice volume, atmospheric CO_2, orbital parameters and freshwater forcing in the framework of self-oscillation.

Chapter 5 Summary and Outlook

In this thesis, we conducted a series of equilibrium or transient model experiments for the end of last ice age with a fully-coupled climate model. The main focus is on impacts of changes in key boundary forcing factors, such as ice volume and atmospheric CO_2 concentration, on AMOC during LGM-HS1-B/A. The main conclusions derived with our model in response to the specific questions in Chapter 1 are as follows:

1. What are the implications of changes in ice sheet and CO_2 for the AMOC strength during the end of the last ice age?

   We suggest that the MWF magnitude to attain and sustain a weak HS type AMOC is modulated by the deglacial ice decline and CO_2 increase. In particular, deglacial ice decline leads to an increased AMOC sensitivity to MWF. Vice versa, a CO_2 rise decreases this sensitivity.

2. What is the response of climate model to reconstructed freshwater forcing resulting from ice sheet retreat?

   In our investigations, ice sheet changes include associated deglacial meltwater and iceberg fluxes based on the state-of-the-art GLAC-1D reconstruction. Where meltwater is distributed to corresponding coastal areas through a surface drainage pointer field, all iceberg fluxes from the Northern Hemisphere enter the North Atlantic Ocean in the IRD belt.

   For 16 ka conditions, a weaker HS-type circulation can be simulated for meltwater fluxes within the range of reconstructions for HS1. Persistent meltwater input below a critical magnitude only causes a temporal weakening of the AMOC, followed by a fast recovery to a strong AMOC state. It appears that the subsurface warming in conjunction with an increase in surface salinity leads to an unstable weak AMOC state with a subsequent B/A-type warming during the last deglaciation.

In the transient framework, a weak freshwater forcing during HS1 and a strong freshwater forcing during B/A prevent the model from accurately reproducing the HS1-B/A transition. The intensity of AMOC is significantly modulated by the amount of freshwater during this period. A significant portion of freshwater is distributed at the shore and thus not enter the main convection area directly. Therefore, to improve the simulation results in the H1, a stronger discharge amount is required. This reflects the critical influence of freshwater distribution on AMOC in the COSMOS model. Considering the two problems of freshwater forcing, we replace the original MWF with the mean state from HS1 to B/A, which effectively increases freshwater in H1 and decreases freshwater in B/A while satisfying the reconstructed ESL uncertainty during this period. Our model shows a stadial climate during H1 and captures the HS1-B/A AMOC recovery based on this strategy. The timing of AMOC recovery here is closely related to the amount of the prescribed freshwater flux.

3. What is the response of AMOC to simultaneous changes in ice sheets and CO_2? What are the effects of other boundary condition changes during this period?

Previous studies have shown that the HS1-B/A transition occurs due to the combined control of CO_2 and ice volume. However, in our sensitivity experiments considering only CO_2 and ice volume change, no AMOC recovery occurred before 13 ka. As the LIS retreats, the southern branch of the westerlies over NA gradually moves northward, facilitating the transport of sea ice generated in the Labrador Sea to NA, preventing the formation of NADW. The reconstructed ice sheet results showed that ice sheet melting started to accelerate after 14.5 ka, and this process can be developed. Model results also suggest that change in CO_2 alone is not sufficient to overcome the potentially strong freshwater forcing and ice-sheet decrease effect and lead to a B/A event during this period.

In addition to the experiments considering ice sheet height changes, AMOC show finally recovers at a different time in sensitivity experiments considering changes in other boundary conditions (CO_2, glacier extent, and orbital parameters). We noticed that except single CO2 forcing experiment, in all the simulations where AMOC mode transition happens, AMOC returns to the weak state after recovery. And in the single orbital forcing and glacial area runs, AMOC enters into the strong mode for the second time. These results indicate that AMOC behavior is characterized by self-oscillation. And this feature has also existed in the full forcing experiment.

4. What is the mechanism for the occurrence of B/A event?

The self-oscillation characterizes the simulated HS1-B/A transition with fixed MWF. The change of orbital parameters during this period may be the reason for the existence of self-oscillation. Meanwhile, the system has the ability to pass the self-oscillation window as other boundary conditions change, especially for the ice sheet. This can be linked to the end of B/A.

Outlook

Current study was conducted with a climate model that excludes the dynamical change of continental ice sheets and were unable to comprehensively examine the climate mechanisms responsible for changes in ice volume response. The interaction between ice sheets and other components also played a critical role in the large-scale reorganization of both atmospheric (Löfverström and Lora, 2017; Roberts et al., 2019) and ocean circulation (Gong et al., 2015). Also, when considering ice sheet meltwater, low-resolution numerical models are unable to accurately resolve narrow coastal flows and mesoscale eddies, leading to a greater diffusion of freshwater into the North Atlantic subpolar region (Condron and Winsor, 2012; Hill and Condron, 2014; Nurser and Bacon, 2014). In addition, the exact location of surface runoff and calving icebergs into the ocean during the last deglaciation is unclear due to the lack of proxy data, and the strength of the AMOC may be extremely sensitive to the freshwater pathways (Lohmann et al., 2020). Thus, in future studies, we would like to further analyze the sequence of deglacial events in climate model setups using interactive ice sheets, explicit ice bergs and finer coastal grid resolution (e.g., Barbi et al., 2014; Lohmann et al., 2020).

On the other hand, as the ice sheets decay, large amounts of freshwater are constantly entering the ocean, resulting in a change in the ocean boundary. This process is particularly evident during the last deglaciation due to the fast melting of the ice sheets. There are studies that consider a time-varying orography in coupled atmosphere–ocean–ice sheet models (e.g., Ridley et al., 2005; Mikolajewicz et al., 2007a, b; Ziemen et al., 2014; Ackermann et al., 2020; Niu et al., 2021) but an interactive ocean bathymetry and coastlines for an ocean model have not been done yet. In standard ESMs, the land-sea mask is traditionally treated as fixed (Meccia & Mikolajewicz, 2018). During the HS1-B/A period considered in this thesis, the ice sheets covering the Nordic Sea and the Barents Sea are no longer connected due to its melting. This can enhance the water exchange between the North Atlantic and the Arctic Ocean, but this process cannot be considered in our current model. Therefore, it is also necessary to consider the changes in the land-sea mask in the future works (e.g., Kapsch et al., 2022).

References

Abelmann, A., Gersonde, R., Knorr, G. *et al.* The seasonal sea-ice zone in the glacial Southern Ocean as a carbon sink. *Nature communications* **6**, 1-13 (2015).

Ackermann, L., Danek, C., Gierz, P., & Lohmann, G. AMOC Recovery in a Multicentennial Scenario Using a Coupled Atmosphere-Ocean-Ice Sheet Model. *Geophysical Research Letters*, **47**, doi: 10.1029/2019GL086810 (2020).

Alley, R. B., Clark, P. U., Keigwin, L. D., & Webb, R. S. Making sense of millennial-scale climate change. *Geophysical Monograph-American Geophysical Union*, **112**, 385-394 (1999).

Banderas, R., Alvarez-Solas, J., Robinson, A. & Montoya, M. An interhemispheric mechanism for glacial abrupt climate change. *Climate Dynamics* **44**, 2897-2908 (2015).

Barbi, D., Lohmann, G., Grosfeld, K. & Thoma, M. Ice sheet dynamics within an Earth system model: coupling and first results on ice stability and ocean circulation, *Geosci. Model Dev.*, **7**, 2003-2013, doi:10.5194/gmd-7-2003-2014 (2014).

Bard, E., F. Rostek, J. L. Turon, & Gendreau, S. Hydrological impact of Heinrich events in the subtropical northeast Atlantic, *Science*, **289**, 1321–1324 (2000).

Barker, S. & Knorr, G. Antarctic climate signature in the Greenland ice core record. *Proceedings of the National Academy of Sciences of the United States of America* **104**, 17278-17282 (2007).

Barker, S., Knorr, G., Edwards, R. L. *et al.* 800,000 years of abrupt climate variability. *Science*, **334**, 347-351 (2011).

Barker, S., Knorr, G., Conn, S. *et al.* Early interglacial legacy of deglacial climate instability. *Paleoceanography and Paleoclimatology*, doi: 10.1029/2019PA003661 (2019).

Barker, S. & Knorr, G. Millennial scale feedbacks determine the shape and rapidity of glacial termination. *Nat Commun*, **12**, doi: 10.1038/s41467-021-22388-6 (2021).

Bereiter, B., Eggleston, S., Schmitt, J. *et al.* Revision of the EPICA Dome C CO_2 record from 800 to 600kyr before present. *Geophys. Res. Lett.* **42**, 542–549, doi: 10.1002/2014GL061957 (2015).

Berger, A. Long-term variations of daily insolation and Quaternary climatic changes. *Journal of the Atmospheric Sciences*, **35**, 2362-2367 (1978).

Böhm, E. Lippold, J., Gutjahr, M. *et al.* Strong and deep Atlantic meridional overturning circulation during the last glacial cycle. *Nature* **517**, 73-76 (2015).

Briggs, R. D., Pollard, D., & Tarasov, L. A data-constrained large ensemble analysis of Antarctic evolution since the Eemian. *QuaternaryScience Reviews*, **103**, 91–115, (2014).

Brovkin, V., Raddatz, T., Reick, C. H., Claussen, M., & Gayler, V. Global biogeophysical interactions between forest and climate. *Geophysical Research Letters*, **36**, (2009).

Buizert, C., Gkinis, V., Severinghaus, J. P. *et al.* Greenland temperature response to climate forcing during the last deglaciation. *Science*, **345**, 1177–1180, doi: 10.1126/science.1254961 (2014).

Clark, P. U., A. M. McCabe, A. C. Mix, & Weaver, A.J. Rapid rise of sea level 19,000 years ago and its global implications, *Science*, **304**, 1141–1144 (2004).

Clark, P. U., Shakun, J. D., Baker, P. A. *et al.* Global climate evolution during the last deglaciation. *Proceedings of the National Academy of Sciences*, **109**, 1134–1142, doi: 10.1073/pnas.1116619109 (2012).

Cheng, H. Edwards, R. L., Sinha, A. *et al.* The Asian monsoon over the past 640,000 years and ice age terminations. *Nature*, **534**, 640-646 (2016).

Condron, A., & Windsor, P. A subtropical fate awaited freshwater discharged from glacial Lake Agassiz. *Geophysical Research Letters*, **38**, L03705, doi: 10.1029/2010GL046011 (2011)

Condron, A. & Winsor, P. Meltwater routing and the Younger Dryas. *Proceedings of the National Academy of Sciences*, **109**, 19928-19933 (2012).

Craig, H. & Gordon, L. I. Deuterium and oxygen 18 variations in the ocean and the marine atmosphere, edited by: Tongiogi, E., Consiglio nazionale delle richerche, Laboratorio de geologia nucleare, Spoleto, Italy, 9–130 (1965).

Dansgaard, W., Johnsen, S. J., Clausen, H. B. *et al.* Evidence for general instability of past climate from a 250-kyr ice-core record. *Nature*, **364,** 218–220, doi: 10.1038/364218a0 (1993).

Deaney, E. D., Barker, S. & Van de Flierdt, T. Timing and nature of AMOC recovery across Termination 2 and magnitude of deglacial CO_2 change. *Nature Communications*, doi: 10.1038/NCOMMS14595 (2017).

Denton, G. H., Anderson, R. F., Toggweiler, J. R. *et al.* The last glacial termination. *science*, **328**, 1652-1656, doi: 10.1126/science.1184119 (2010).

Deschamps, P., Durand, N., Bard, E. *et al.* Ice-sheet collapse and sea-level rise at the Bølling warming 14,600 years ago, *Nature*, **483**, 559–564, doi: 10.1038/nature10902 (2012).

Dima, M., Lohmann, G. & Knorr, G. North Atlantic Versus Global Control on Dansgaard-Oeschger Events. *Geophysical Research Letters*, **45**, 12,991-912,998 (2018).

Fairbanks, R. G., & Wright, C. C. J. Origin of global meltwater pulses. Radiocarbon after four decades. Springer, New York, NY, 473-500 (1992).

Ganopolski, A. & Roche, D. M. On the nature of lead-lag relationships during glacial-interglacial climate transitions.

Quat. Sci. Rev., **28**, 3361–3378, doi: 10.1016/j.quascirev.2009.09.019 (2009).

Galbraith, E. & de Lavergne, C. Response of a comprehensive climate model to a broad range of external forcings: relevance for deep ocean ventilation and the development of late Cenozoic ice ages. *Climate Dynamics*, **52**, 653-679 (2019).

Gong, X., Knorr, G., Lohmann, G., & Zhang, X. Dependence of abrupt Atlantic meridional ocean circulation changes on climate background states. *Geophysical Research Letters*, **40**, 3698-3704 (2013).

Gong, X., Zhang, X., Lohmann, G., Wei, W., Zhang, X., & Pfeiffer, M. Higher Laurentide and Greenland ice sheets strengthen the North Atlantic ocean circulation, *Climate Dynamics*, **45**, 139–150, doi: 10.1007/s00382-015-2502-8 (2015).

Hagemann, S., & L. Dümenil, A parametrization of the lateral waterflow for the global scale, *Clim. Dyn.*, **14**, 17-31 (1998).

Hagemann, S., & L. D. Gates, Improving a subgrid runoff parameterization scheme for climate models by the use of high resolution data derived from satellite observations, *Clim. Dyn.*, **21**, 349–359, doi: 10.1007/s00382-003-0349-x (2003).

He, F., Shakun, J. D., Clark, P. U., Carlson, A. E., Liu, Z., Otto-Bliesner, B. L., & Kutzbach, J. E. Northern Hemisphere forcing of Southern Hemisphere climate during the last deglaciation. *Nature*, **494**, 81–85 (2013).

Hemming, S. R. Heinrich events: Massive late Pleistocene detritus layers of the North Atlantic and their global climate imprint. *Reviews of Geophysics*, **42** (2004).

Hibler III, W. A dynamic thermodynamic sea ice model. *Journal of physical oceanography*, **9**, 815–846 (1979).

Hill, J. C. & Condron, A. Subtropical iceberg scours and meltwater routing in the deglacial western North Atlantic, *Nat. Geosci.*, **7**, 806–810, doi: 10.1038/ngeo2267 (2014).

Hossain, A., Knorr, G., Lohmann, G., Stärz, M., & Jokat, W. Simulated thermohaline fingerprints in response to different Greenland-Scotland Ridge and Fram Strait subsidence histories. *Paleoceanography and Paleoclimatology*, **35**, e2019PA003842 (2020).

Huang, X., M. Stärz, K. Gohl, G. Knorr & Lohmann, G., Impact of Weddell Sea shelf progradation on Antarctic bottom water formation during the Miocene. *Paleoceanography*, **32**, doi: 10.1002/2016PA002987 (2017).

Imbrie, J., Berger, A., Boyle, E. *et al.* On the structure and origin of major glaciation cycles 2. the 100,000-year cycle. *Paleoceanography*, **8**, 699-735 (1993).

Ivanovic, R. F., Gregoire, L. J., Kageyama, M. *et al.* Transient climate simulations of the deglaciation 21–9 thousand years before present (version 1) – PMIP4 core experiment design and boundary conditions. *Geoscientific Model Development*, **9**, 2563– 2587, doi: 10.5194/gmd-9-2563-2016 (2016)

Jouzel, J., Masson-Delmotte, V., Cattani, O. *et al.* Orbital and millennial Antarctic climate variability over the past 800,000 years. *science*, **317**, 793-796 (2007).

Jungclaus, J. H., Keenlyside, N., Botzet, M. *et al.* Ocean circulation and tropical variability in the coupled model ECHAM5/MPI-OM. *Journal of climate*, **19**, 3952-3972 (2006).

Jungclaus, J. H., Lorenz, S. J., Timmreck, C. *et al.* Climate and carbon-cycle variability over the last millennium. *Climate of the Past*, **6**, 723–737 (2010).

Kapsch, M. L., Mikolajewicz, U., Ziemen, F., & Schannwell, C. Ocean Response in Transient Simulations of the Last Deglaciation Dominated by Underlying Ice-Sheet Reconstruction and Method of Meltwater Distribution. *Geophysical Research Letters*, **49**, doi: 10.1029/2021GL096767 (2022).

Kim, J.-H., Romero, O. E., Lohmann, G., Donner, B., Laepple, T., Haam, E., & Damsté, J. S. S. Pronounced subsurface cooling of North Atlantic waters off northwest Africa during Dansgaard-Oeschger interstadials. *Earth and Planetary Science Letters*, **339-340**, 95–102 (2012).

Kindler, P., Guillevic, M., Baumgartner, M., Schwander, J., Landais, A., & Leuenberger, M. Temperature reconstruction from 10 to 120 kyr b2k from the NGRIP ice core. *Climate of the Past*, **10**, 887-902 (2014).

Klockmann, M., Mikolajewicz, U. & Marotzke, J. The effect of greenhouse gas concentrations and ice sheets on the glacial AMOC in a coupled climate model. *Climate of the Past*, **12**, 1829-1846 (2016).

Klockmann, M., Mikolajewicz, U. & Marotzke, J. Two AMOC states in response to decreasing greenhouse gas concentrations in the coupled climate model MPI-ESM. *Journal of Climate*, **31**, 7969-7984 (2018).

Knorr G & Lohmann G. Southern Ocean origin for the resumption of Atlantic thermohaline circulation during deglaciation. *Nature*, **424**, 532-536, doi: https://doi.org/10.1038/nature01855 (2003).

Knorr, G. & Lohmann, G. Rapid transitions in the Atlantic thermohaline circulation triggered by global warming and meltwater during the last deglaciation. *Geochemistry, Geophysics, Geosystems*, **8**, doi: 10.1029/2007GC001604 (2007).

Knorr, G., Butzin, M., Micheels, A., & Lohmann, G. A warm Miocene climate at low atmospheric CO_2 levels. *Geophysical Research Letters*, **38**, (2011).

Knorr, G., & Lohmann, G. Climate warming during Antarctic ice sheet expansion at the Middle Miocene transition. *Nature Geoscience*, **7**, 376-381 (2014).

Knorr, G., Barker, S., Zhang, X., Lohmann, G., Gong, X., Gierz, P., Stepanek, C. & Stap, L. B. A salty deep ocean as a prerequisite for glacial termination. *Nat. Geosci.*, **14,** 930–936, doi: 10.1038/s41561-021-00857-3 (2021).

Köhler, P., Nehrbass-Ahles, C., Schmitt, J., Stocker, T. F., & Fischer, H. A 156 kyr smoothed history of the atmospheric greenhouse gases CO2, CH4, and N2O and their radiative forcing. *Earth System Science Data*, **9**, 363-387 (2017).

Li, C. & Born, A. Coupled atmosphere-ice-ocean dynamics in Dansgaard-Oeschger events. *Quaternary Science Reviews*, **203**, 1–20. Doi: 10.1016/j.quascirev.2018.10.031 (2019).

Liu, Z., Otto-Bliesner, B. L., He, F. *et al.* Transient Simulation of Last Deglaciation with a New Mechanism for Bølling-Allerød Warming. *Science*, **325**, 310-314 (2009).

Lohmann, G. & Schulz, M. Reconciling Bølling warmth with peak deglacial meltwater discharge. *Paleoceanography*, **15,** 537-540 (2000).

Lohmann, G. Atmospheric and oceanic freshwater transport during weak Atlantic overturning circulation. *Tellus*, **55 A**, 438-449 (2003).

Lohmann, G., Butzin, M., Eissner, N., Shi, X. & Stepanek C. Abrupt climate and weather changes across timescales. *Paleoceanography and Paleoclimatology*, **35,** e2019PA003782, doi: 10.1029/2019PA003782 (2020).

Lohmann, G., Knorr, G., Hossain, A. & Stepanek C. Effects of CO2 and ocean mixing on Miocene and Pliocene temperature gradients. *Paleoceanography and Paleoclimatology*, **37**, doi: 10.1029/2020PA003953 (2022).

Loulergue, L., Schilt, A., Spahni, R. *et al.* Orbital and millennial-scale features of atmospheric CH_4 over the past 800,000 years. *Nature*, **453,** 383–386, doi: 10.1038/nature06950 (2008).

Lott, F. & Miller, M. J. A new-subgrid-scale orographic drag parameterization: Its formulation and testing. *Quart. J. Roy. Meteor. Soc.*, **123**, 101–127 (1997).

Lott, F. Alleviation of stationary biases in a GCM through a mountain drag parameterization scheme and a simple representation of mountain lift forces. Mon. Wea. Rev., **127**, 788–801 (1999).

Löfverström, M., & Lora, J. M. Abrupt regime shifts in the North Atlantic atmospheric circulation over the last deglaciation. *Geophysical Research Letters*, **44**, 8047–8055, doi: 10.1002/2017gl074274 (2017).

Manabe, S. & Stouffer, R. J. Coupled ocean-atmosphere model response to freshwater input: Comparison to Younger Dryas event. *Paleoceanography*, **12**, 321-336 (1997).

Marsland, S. J., Haak, H., Jungclaus, J. H., Latif, M., & Röske, F. The Max-Planck-Institute global ocean/sea ice model with orthogonal curvilinear coordinates. *Ocean modelling*, **5**, 91-127 (2003).

McManus, J. F., Francois, R., Gherardi, J. M., Keigwin, L. D. & Brown-Leger, S. Collapse and rapid resumption of Atlantic meridional circulation linked to deglacial climate changes. *Nature*, **428**, 834-837 (2004).

Meccia, V. L. & Mikolajewicz, U. Interactive ocean bathymetry and coastlines for simulating the last deglaciation with the Max Planck Institute Earth System Model (MPI-ESM-v1. 2). *Geoscientific Model Development*, **11**, 4677-4692 (2018).

Menviel, L., Timmermann, A., Timm, O. E., & Mouchet, A. Deconstructing the last glacial termination: The role of millennial and orbital-scale forcings. *Quaternary Science Reviews*, **30,** 1155–1172 (2011)

Mikolajewicz, U., Gröger, M., Maier-Reimer, E., Schurgers, G., Vizcaíno, M., & Winguth, A. M. Long-term effects of anthropogenic CO_2 emissions simulated with a complex earth system model, *Clim. Dynam.*, **28**, 599–633, doi: 10.1007/s00382-006-0204-y (2007a).

Mikolajewicz, U., Vizcaino, M., Jungclaus, J., & Schurgers, G. Effect of ice sheet interactions in anthropogenic climate change simulations, *Geophys. Res. Lett.*, **34**, doi: 10.1029/2007GL031173 (2007b).

Muglia, J. & Schmittner, A. Glacial Atlantic overturning increased by wind stress in climate models. *Geophysical Research Letters*, **42**, 9862-9868 (2015).

NEEM community members. Eemian interglacial reconstructed from a Greenland folded ice core. *Nature*, **493,** 489–494, doi: 10.1038/nature11789 (2013).

Ng, H. C., Robinson, L. F., McManus, J. F., Mohamed, K. J., Jacobel, A. W., Ivanovic, R. F., Gregoire, L. J. & Chen, T. Coherent deglacial changes in western Atlantic Ocean circulation. *Nature Communications*, **9**, doi: /10.1038/s41467-018-05312-3 (2018).

Niu, L., Lohmann, G., Gierz, P., Gowan, E. J., & Knorr, G. Coupled climate-ice sheet modelling of MIS-13 reveals a sensitive Cordilleran Ice Sheet. *Global and Planetary Change*, **200**, doi: 10.1016/j.gloplacha.2021.103474 (2021).

North Greenland Ice Core Project members. High-resolution record of Northern Hemisphere climate extending into the last interglacial period. *Nature*, **431,** 147–151, doi: 10.1038/nature02805 (2004).

Nurser, A. J. G. & Bacon, S. The Rossby radius in the Arctic Ocean, *Ocean Sci.*, **10**, 967–975, doi: 10.5194/os-10-967-2014 (2014).

Obase, T., & Abe-Ouchi, A. Abrupt Bølling-Allerød warming simulated under gradual forcing of the last deglaciation. *Geophysical Research Letters*, **46**, 11,397–11,405. https://doi.org/10.1029/2019GL084675 (2019).

Oka, A., Hasumi, H. & Abe-Ouchi, A. The thermal threshold of the Atlantic meridional overturning circulation and its control by wind stress forcing during glacial climate. *Geophysical Research Letters*, **39** (2012).

Otto-Bliesner, B. L. & Brady, E. C. The sensitivity of the climate response to the magnitude and location of freshwater forcing: last glacial maximum experiments, *Quaternary Sci. Rev.*, **29**, 56–73, doi: 10.1016/j.quascirev.2009.07.004 (2010).

Pedro, J. B., Bostock, H. C., Bitz, C. M., He, F., Vandergoes, M. J., Steig, E. J., Chase, B. S., Krause, C. E., Rasmussen, S. O., Markle, B. R. & Cortese, G. The spatial extent and dynamics of the Antarctic cold reversal. *Nature Geoscience*, **9**, 51–56, doi: 10.1038/NGEO2580 (2016).

Peltier, W. R., Vettoretti, G., & Stastna, M. Atlantic meridional overturning and climate response to Arctic Ocean freshening. *Geophysical Research Letter*s, **33**, doi: 10.1029/2005GL025251 (2006).

Raddatz, T. J., Reick, C. H., Knorr, W., Kattge, J., Roeckner, E., Schnur, R., Schnitzler, K.-G., Wetzel, P. & Jungclaus, J. Will the tropical land biosphere dominate the climate–carbon cycle feedback during the twenty-first century? *Climate Dynamics*, **29**, 565-574 (2007).

Rahmstorf, S. Ocean circulation and climate during the past 120,000 years. *Nature*, **419,** 207–214, doi: 10.1038/nature01090 (2002).

Raymo, M. E. The timing of major climate terminations. *Paleoceanography*, **12**, 577-585 (1997).

Ridley, J. K., Huybrechts, P., Gregory, J. U., & Lowe, J. A. Elimination of the Greenland Ice Sheet in a High CO_2 Climate, *J. Climate*, **18**, 3409–3427, doi: 10.1175/JCLI3482.1 (2005).

Roberts, N. L., Piotrowski, A. M., McManus, J. F. & Keigwin, L. D. Synchronous Deglacial Overturning and Water Mass Source Changes. *Science*, **327**, 75-78 (2010).

Roberts, W. H., Li, C., & Valdes, P. J. The mechanisms that determine the response of the Northern Hemisphere's stationary waves to North American ice sheets, *Journal of Climate*, **32**, 3917–3940, doi: 10.1175/JCLI-D-18-0586.1 (2019).

Roeckner, E., Bauml, G., Bonaventura, L., & Brokopf, R. The general circulation model ECHAM5. Part I: Model description. Hamburg, Germany, Max-Planck-Institute for Meteorology (2003).

Rühlemann, C., Mulitza, S., Lohmann, G., Paul, A., Prange, M., & Wefer, G. Intermediate depth warming in the tropical Atlantic related to weakened thermohaline circulation: Combining paleoclimate and modeling data for the last deglaciation. *Paleoceanography*, **19**, PA1025, doi: 10.1029/2003PA000948 (2004).

Sarnthein, M., Winn, K., Jung, S. J., Duplessy, J. C., Labeyrie, L., Erlenkeuser, H., & Ganssen, G. Changes in east Atlantic deepwater circulation over the last 30,000 years: Eight time slice reconstructions. *Paleoceanography*, **9**, 209–267 (1994).

Schilt, A., Baumgartner, M., Schwander, J., et al., *Earth Planet. Sci. Lett.*, **300**, 33–43, doi: 10.1016/j.epsl.2010.09.027 (2010).

Shakun, J. D., & Carlson, A. E. A global perspective on Last Glacial Maximum to Holocene climate change. *Quaternary Science Reviews*, **29**, 1801–1816, doi: 10.1016/j.quascirev.2010.03.016 (2010).

Sherriff-Tadano, S., Abe-Ouchi, A., Yoshimori, M., Oka, A. & Chan, W.-L. Influence of glacial ice sheets on the Atlantic meridional overturning circulation through surface wind change. *Climate Dynamics*, **50**, 2881-2903 (2018).

Simon, M. H., Gong, X., Hall, I. R., Ziegler, M., Barker, S., Knorr, G., van der Meer, M. T., Kasper, S. & Schouten, S. Salt exchange in the Indian-Atlantic Ocean Gateway since the Last Glacial Maximum: A compensating effect between Agulhas Current changes and salinity variations? *Paleoceanography*, **30**, 1318-1327, doi: 10.1002/2015PA002842 (2015).

Stepanek, C., Samakinwa, E., Knorr, G., and Lohmann, G. Contribution of the coupled atmosphere–ocean–sea ice–vegetation model COSMOS to the PlioMIP2, *Clim. Past*, **16**, 2275–2323, doi: 10.5194/cp-16-2275-2020 (2020).

Stocker, T. F. Past and future reorganizations in the climate system. *Quaternary Science Reviews*, **19**, 301-319 (2000).

Sun, Y., Knorr, G., Zhang, X., Tarasov, L., Barker, S., Werner, M., & Lohmann, G. Ice sheet decline and rising atmospheric CO_2 control AMOC sensitivity to deglacial meltwater discharge. *Global and Planetary Change*, **210**, doi: 10.1016/j.gloplacha.2022.103755 (2022).

Tarasov, S., Arthur S. Dyke, Radford M. Neal & Peltier, W.R. A data-calibrated distribution of deglacial chronologies for the North American ice complex from glaciological modeling, *Earth and Planetary Science Letters*, **315**, 30–40 (2012).

Tarasov, L., Hughes, A., Gyllencreutz, R., Lohne, O.S., Mangerud, J, & Svendsen, J.I. The global GLAC-1c deglaciation chronology, melwater pulse 1-a, and a question of missing ice. IGS Symposium on Contribution of Glaciers and Ice Sheets to Sea-Level Change (2014).

Valcke, S. *et al.* OASIS3 Users's Guide, CERFACS, Toulouse, France (2003).

Venz, K. A., Hodell, D. A., Stanton, C. & Warnke, D. A. A 1.0 Myr record of glacial North Atlantic intermediate water variability from ODP site 982 in the northeast Atlantic. *Paleoceanography*, **14**, 42-52 (1999).

Wei, W., Lohmann, G., & Dima, M. Distinct modes of internal variability in the global meridional overturning circulation associated with the Southern Hemisphere westerly winds. *Journal of Physical Oceanography*, **42**, 785-801 (2012).

Wei, W., & Lohmann, G. Simulated Atlantic multidecadal oscillation during the Holocene. *Journal of Climate*, **25**, 6989-7002 (2012).

Werner, M., Haese, B., Xu, X., Zhang, X., Butzin, M., & Lohmann, G. Glacial–interglacial changes in $H_2^{18}O$, HDO and deuterium excess–results from the fully coupled ECHAM5/MPI-OM Earth system model. *Geoscientific Model Development*, **9**, 647-670 (2016).

Zhang, X., Lohmann, G., Knorr, G., & Xu, X. Different ocean states and transient characteristics in Last Glacial Maximum simulations and implications for deglaciation. *Climate of the Past*, **9**, 2319-2333 (2013).

Zhang, X., Lohmann, G., Knorr, G. & Purcell, C. Abrupt glacial climate shifts controlled by ice sheet changes. *Nature*, **512**, 290-294 (2014).

Zhang, X., Knorr, G., Lohmann, G. & Barker, S. Abrupt North Atlantic circulation changes in response to gradual CO_2 forcing in a glacial climate state. *Nature Geoscience*, **10**, 518-523, doi:10.1038/ngeo2974 (2017).

Zhang, X., Barker, S., Knorr, G., Lohmann, G., Drysdale, R., Sun, Y., Hodell, D. & Chen, F. Direct astronomical influence on abrupt climate variability. *Nat. Geosci.*, **14**, 819–826, doi: 10.1038/s41561-021-00846-6 (2021).

Zhu, J., Z. Liu, X. Zhang, I. Eisenman, & Liu, W. Linear weakening of the AMOC in response to receding glacial ice sheets in CCSM3, *Geophysical Research Letters*, **41**, 6252–6258, doi:10.1002/ 2014GL060891 (2014).

Ziemen, F. A., Rodehacke, C. B., & Mikolajewicz, U. Coupled ice sheet-climate modeling under glacial and pre-industrial boundary conditions, *Clim. Past*, **10**, 1817–1836, doi: 10.5194/cp-10-1817-2014 (2014).